

TIME-DEPENDENT COOLING IN PHOTOIONIZED PLASMA

ORLY GNAT¹

ACCEPTED TO APJS: December 20, 2016

ABSTRACT

I explore the thermal evolution and ionization states in gas cooling from an initially hot state in the presence of external photoionizing radiation. I compute the equilibrium and nonequilibrium cooling efficiencies, heating rates, and ion fractions for low-density gas cooling while exposed to the ionizing metagalactic background radiation at various redshifts ($z = 0 - 3$), for a range of temperatures ($10^8 - 10^4$ K), densities ($10^{-7} - 10^3$ cm⁻³) and metallicities ($10^{-3} - 2$ times solar). The results indicate the existence of a threshold ionization parameter, above which the cooling efficiencies are very close to those in photoionization equilibrium (so that departures from equilibrium may be neglected), and below which the cooling efficiencies resemble those in collisional time-dependent gas cooling with no external radiation (and are thus independent of density).

Subject headings: ISM:general – atomic processes – plasmas – absorption lines – intergalactic medium

1. INTRODUCTION

The radiative cooling efficiencies of low-density plasma are necessary quantities in the study of diffuse gas in and around galaxies. They are important in setting the rates at which gas accretes onto, and is ejected from, forming galaxies, and are therefore essential for modeling various aspects of galaxy formation and evolution.

The time-dependent radiative cooling of highly ionized gas, in the absence of any external sources of heating or photoionization, is a well-studied problem dating back to Kafatos (1973), that has been revisited by many other authors. Here I refer to such conditions as “collisional”, as opposed to “photoionized” gas. In photoionized gas non-collisional (i.e. radiative) processes become significant. Gnat & Sternberg (2007, hereafter GS07) studied the time-dependent ionization and cooling in collisional plasma. They calculated the equilibrium and nonequilibrium ionization states and radiative cooling efficiencies of low density gas cooling from an initial hot temperature. With no radiation, the collisional ionization *equilibrium* (CIE) ion fractions and radiative cooling efficiencies are functions of the temperature only.

In GS07 the main emphasis has been on the departures from equilibrium that occur when the cooling time becomes short compared with the electron-ion recombination time in collisional plasma. Below $\sim 5 \times 10^6$ K, recombination becomes slow compared with cooling, and so the plasma tends to remain more highly ionized than expected for CIE. More highly ionized species generally have more energetic resonance line transitions, and so thermal electrons are less efficient in exciting over-ionized plasma, causing a suppression of the cooling efficiency at any temperature. Because metal-lines dominate the cooling over a wide range of temperatures, departures from equilibrium are more prominent for high-metallicity gas.

In astrophysical environments, low-density gas rarely exists in the absence of significant sources of ionizing radiation, either stellar or extragalactic. This radiation

modifies the ionization states, thus directly affecting the observational signatures. For example, photoionizing radiation is key to understanding the absorption line signatures from circum-galactic gas (Churchill et al. 2015; Crighton et al. 2015); the origin of cold gas in galactic winds (Thompson et al. 2015); and the physical properties of gas around star-forming galaxies (Turner et al. 2015);

Crucially, when photoionization modifies the ionization states, it affects the cooling efficiencies which in turn determine the rates and epochs at which galaxies accrete their gas (this idea dates back to white & Rees 1978). At high redshifts, where the IGM is composed of primordial gas, photoionizing radiation has been shown to suppress cooling significantly, thus quenching the formation rate of low-mass galaxies (e.g. Efstathiou 1992). More recent studies have shown that higher-mass galaxies also have their gas accretion- and star formation-rates regulated by the photoionizing radiation (e.g., Navarro & Steinmetz 1997; Benson et al. 2002a; 2002b; 2003; Cantalupo 2010. See, however, Weinberg et al. 1997). The photoionized cooling efficiencies are therefore key to understanding both galaxy- and star-formation.

The ionization states in photoionization equilibrium have been studied extensively (E.g. recently by Churchill et al. 2014). The cooling and heating functions in photoionization equilibrium have been recently studied by Gnedin & Hollon (2012; for stellar and AGN spectral energy distributions) and Wiersma et al. (2009; for the CMB and metagalactic background). The nonequilibrium radiative cooling of hot ($> 10^4$ K) *photoionized* gas, and the associated time-dependent ionization of the metal ions have been recently considered by Vasiliev (2011) and by Oppenheimer & Schaye (2013). Oppenheimer & Schaye (2013) presented results for gas densities between 10^{-5} and 10^{-2} cm⁻³, and for gas metallicities between 0.1 and 2 times solar. Departures from equilibrium cooling has been shown to affect the temperature of the IGM (Punchwein et al. 2015); the UV absorption signatures in the proximity of AGN (Oppenheimer & Schaye 2013); and the composition of galactic outflows (Richings & Schaye 2015);

orlyg@phys.huji.ac.il

¹Racah Institute of Physics, The Hebrew University, Jerusalem 91904, Israel

In this paper, I reexamine the fundamental problem of nonequilibrium ionization of a time-dependent radiatively cooling gas in the presence of external photoionization. I focus on the impact that the photoionizing background has on the thermal evolution and ionization states. I consider the metagalactic background radiation (Haardt & Madau 2012, hereafter HM12) for redshifts between 0 and 3, gas densities between 10^{-7} and 10^3 cm^{-3} , and metallicities between 10^{-3} and 2 times solar. When photoionization and heating by the metagalactic background affect the physical properties of the cooling gas, the conditions become functions of the temperature, metallicity *and density* (or, equivalently, ionization parameter) of the gas.

The computations presented here indicate the existence of a threshold ionization parameter, above which the nonequilibrium cooling efficiencies are very close to those in photoionization equilibrium (so that departures from equilibrium may be neglected), and below which the cooling efficiencies resemble those in collisional time-dependent gas cooling with no external radiation (and are thus independent of density).

The outline of this paper is as follows. In §2 (and Appendix A) I summarize the numerical method and physical ingredients included in this computation. In §3 I describe how the photoionizing radiation affects the thermal evolution of radiatively cooling gas. I compare the equilibrium and nonequilibrium cooling efficiencies, and identify the threshold ionization parameter that separates the regime of photoionization equilibrium from the regime of time-dependent collisional cooling. §4 presents the ionization states as functions of gas temperature and density, for both photoionization equilibrium and nonequilibrium cooling. The full set of results, for metallicities 10^{-3} - 2 times solar, and for densities between 10^{-7} and 10^3 cm^{-3} , are available as online data files. In §5 I discuss the evolution of the density ratios C IV/O VI versus N V/O VI in photoionized cooling gas. This density ratio can be used as a diagnostic tool for photoionized plasma. Additional diagnostic diagrams can be constructed using the online data presented in this paper. I summarize in §6.

2. NUMERICAL METHOD AND PROCESSES

The goal of this paper is to study how an external radiation field affects the observational signatures in radiatively cooling plasma. I consider gas which is initially heated to a temperature $\gtrsim 5 \times 10^6 \text{ K}$, and then cools radiatively. As in GS07, at the initial hot state, cooling is slower than recombination, and so the gas can reach ionization equilibrium before significant cooling takes place. As opposed to the situation discussed in GS07, here the gas is exposed to a continuous and constant source of heating and photoionization as it cools. The initial ionization equilibrium state is that of *photoionization* equilibrium (as opposed to CIE in GS07). In all cases considered here, the heating rate at the initial photoionization equilibrium state is lower than the cooling rate, and therefore the gas is not in *thermal* equilibrium, and will cool radiatively until the condition of thermal equilibrium is satisfied. I compute the coupled time-dependent evolution for clouds cooling at constant density (see §3.1 for a discussion of isobaric evolution), for a wide range of metallicities, taking into account departures from pho-

toionization equilibrium.

In my computations I follow the numerical scheme outlined in GS07 and improved in Gnat & Sternberg (2009). The details of this numerical method and computational ingredients are summarized in Appendix A. I consider all ionization stages of the elements H, He, C, N, O, Ne, Mg, Si, S, and Fe. I include photoionization, collisional ionization by thermal electrons, radiative recombination, dielectronic recombination, neutralization and ionization by charge transfer reactions with hydrogen and helium atoms and ions, and multi electron Auger ionization processes. The photoionization rates are due to the externally incident radiation.

The ionization equations are coupled to an energy equation for the time-dependent heating and cooling, and resulting temperature variation. I follow the electron cooling efficiency, $\Lambda(T, x_i, Z)$ ($\text{erg s}^{-1} \text{ cm}^3$), and the heating rate $\Upsilon(J_\nu, x_i, Z)$ (erg s^{-1}), which depend on the gas temperature, the photoionizing background, the ionization state, and the metallicity Z . As in GS07, I adopt the elemental abundances reported by Asplund et al. (2005) for the photosphere of the Sun, and the enhanced Ne abundance recommended by Drake & Testa (2005; see Table 1 in GS07). In all computations I assume a primordial helium abundance $A_{\text{He}} = 1/12$ (Ballantyne et al. 2000), independent of Z .

The electron cooling efficiency includes the removal of electron *kinetic* energy² via recombination with ions, collisional ionization, collisional excitation followed by prompt line emission, thermal bremsstrahlung (GS07), and Compton cooling off the metagalactic background radiation. The compton cooling power is given by

$$P_{\text{compton}} = \left(\frac{4kT}{m_e c} \right) \sigma_T n_e \Phi_{\text{ph}}, \quad (1)$$

where,

$$\Phi_{\text{ph}} = \frac{4\pi}{c} \int_0^\infty J_\nu d\nu. \quad (2)$$

Most of the cooling processes (line-emission, recombinations, ionization, thermal bremsstrahlung) are two-body processes, and are therefore proportional to the density squared for the low densities considered here ($10^{-7} - 10^3 \text{ cm}^{-3}$). However, Compton cooling is proportional to the electron density times the photon density, and therefore dominates at low densities, where all other processes are suppressed.

For the heating rate, $\Upsilon(x_i, Z, J_\nu)$ (erg s^{-1}) I include compton heating by high energy photons and photoionization by the background radiation, J_ν . Each photoionizing photon adds an energy $h\nu_\gamma - h\nu_{\text{IP}}$ to the kinetic energy of the electron gas, where ν_γ is the absorbed photon frequency, and ν_{IP} is the ionization threshold of the ionized ion.

The cooling efficiencies and heating rates were computed by passing the nonequilibrium ion fractions $x_i(T)$ to the Cloudy cooling and heating functions. The results presented here have been obtained using Cloudy version 13.00. The net local cooling rate per volume is given by $n_e n_H \Lambda_{e,H} - n_H \Upsilon$.

² I do not include the ionization potential energies as part of the internal energy but instead follow the loss and gain of the electron kinetic energy only.

For an ideal gas, the pressure $P = nk_B T$, and the thermal energy density $u = 3/2nk_B T$. If dQ is the amount of heat lost (or gained) by the thermal electron gas, then for isochoric cooling (for which $dV = 0$),

$$dQ = dU = \frac{3}{2}(Nk_B dT + k_B T dN) \quad (3)$$

This leads to the relation,

$$\frac{3}{2} \frac{dP}{dt} = -n_e n_H \Lambda(T, x_i, Z) + n_H \Upsilon(J_\nu, x_i, Z) \quad (4)$$

(GS07, Kafatos 1973).

In the absence of external radiation (i.e. when $\Gamma_i = 0$ and $\Upsilon = 0$) the evolution of the ion fractions as functions of temperature, $\frac{dx_i}{dT} = (\frac{dx_i}{dF})/(\frac{dT}{dt})$, is independent of the gas density or pressure. When external radiation is present, the ion fractions at a given temperature and ionizing background are functions of the gas density or, equivalently, of the ionization parameter,

$$U = \frac{4\pi}{n_e c} \int_{\nu_0}^{\infty} \frac{J_\nu}{h\nu} d\nu \quad (5)$$

which measures the ratio of the ionizing photon density to the electron density.

The ionic rate equations and energy-balance equation (4) constitute a set of 103 coupled ordinary differential equations (ODEs). I use the numerical scheme outlined in GS07 for isochorically cooling gas to solve for the non-equilibrium ion-fractions and temperature. Here the local errors for hydrogen, helium, and metal ions were set to be smaller than 10^{-9} , 10^{-8} , and 10^{-7} , respectively. The high accuracy is crucial, because heating is sometimes dominated by trace species. The integration has been carried out to a minimum temperature T_{low} , set by the condition of thermal equilibrium with the background radiation field. If the equilibrium temperature is lower than 10^4 K, I set $T_{\text{low}} = 10^4$ K, because molecular chemistry and dust cooling are not included in this work, and the results for temperatures below 10^4 K may therefore be unreliable.

3. COOLING EFFICIENCIES

In this section I describe the thermal evolution of the cooling gas, and examine its dependence on the controlling parameters: the ionizing radiation, gas density, and metallicity.

For the photoionizing radiation field, I consider the metagalactic background radiation at redshifts, $z = 0, 0.5, 1, 2,$ and 3 (HM12), between 0.009 and $\sim 6 \times 10^5$ Ryd (~ 0.1 eV– $8,330$ keV). I show the full HM12 spectral energy distributions in Figure 1. The mean intensity of the metagalactic background increases between redshift 0 and 2. It reaches a maximum at $z \sim 2$ and then decreases again at higher redshifts. The ionizing photon densities ($4\pi/c \int J_\nu/h\nu d\nu$) are listed in Table 1.

I consider gas densities between 10^{-7} cm^{-3} (\sim the cosmic mean) and 10^3 cm^{-3} , and explore five different values of gas metallicity from 10^{-3} to 2 times the metal abundance of the sun. For each redshift-density-metallicity combination, I have carried out computations of the ion fractions, cooling efficiencies and heating rates as functions of gas temperature. First, I assume photoionization equilibrium (hereafter PIE, see Table 2) imposed at

TABLE 1
IONIZING PHOTON
DENSITY IN HM12 SEDS

Redshift	$n_\gamma = U n_H$
0	4.2×10^{-6}
0.5	2.2×10^{-5}
1	7.8×10^{-5}
2	1.6×10^{-4}
3	1.4×10^{-4}

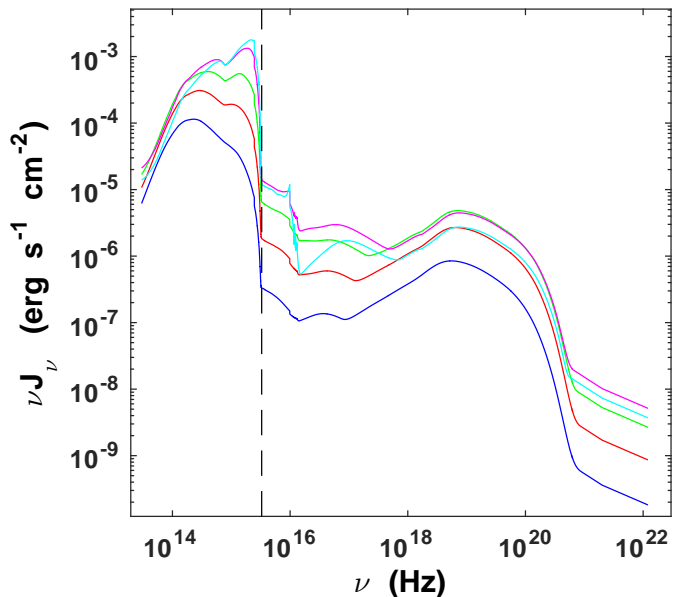


FIG. 1.— Mean intensity versus frequency in the Haardt & Madau (2012) background radiation at $z = 0, 0.5, 1, 2,$ and 3 . The mean intensity of ionizing photons rises from $z = 0$ to $z = 2$, and then decreases for higher redshifts. The dashed curve shows the Lyman limit.

all temperatures to calculate the PIE ion fractions and cooling efficiencies. Then I consider the non-equilibrium evolution of photoionized cooling gas, to compute the time-dependent ionization and cooling.

Here I focus on the total cooling efficiencies, $\Lambda_{H,e}(z, Z, T)$ ($\text{ergs cm}^3 \text{ s}^{-1}$), in the photoionized cooling gas. Figure 2 shows the cooling efficiencies as a function of gas temperature for solar metallicity gas. Panel (a) shows the cooling for collisional plasma, i.e., with no external radiation (GS07). The blue solid curve is for CIE. This familiar curve shows the hydrogen Ly α peak at $\sim 10^4$ K, followed by dominant contributions from carbon, oxygen, neon and iron resonance-lines, and thermal bremsstrahlung (from low to high temperature). The black dashed curve is for time-dependent collisional cooling (hereafter TDC, see Table 2). The narrow contributions dominated by individual species that appear for CIE are smeared out in the TDC curves. This is due to the broader ion distribution that occur as overionized species persist down to low temperatures. The nonequilibrium collisional cooling efficiencies are suppressed, by factors of 2–4, compared to CIE cooling. This is because the gas remains "overionized" as it cools, and consequently tends to have more energetic resonance line transitions (McCray 1987), which are less accessible to

TABLE 2
ACRONYM GLOSSARY

Processes	Equilibrium	Time-Dependent
Collisional Only	CIE	TDC
	Collisional Ionization Equilibrium	Time-Dependent Collisional
Including Radiation	PIE	TDP
	Photo-Ionization Equilibrium	Time-Dependent Photoionized

the “cooler” thermal electrons.

Panel (b) compares the CIE cooling curve (again, solid blue) with the cooling efficiencies assuming PIE in a 10^{-5} cm^{-3} gas in the presence of the $z = 0$ HM12 metagalactic radiation field (dash-dotted magenta curve). Photoionized gas is more highly ionized than gas in collisional equilibrium because of the additional ionization term due to radiation. Just as in the case of departures from equilibrium, the more highly ionized species are less efficiently excited by the thermal electrons, and cooling is suppressed.

Finally, panel (c) compares the *non-equilibrium* cooling efficiencies in the collisional case (TDC, dashed black) and in the photoionized case (solid red) assuming 10^{-5} cm^{-3} gas in the presence of the $z = 0$ HM12 metagalactic radiation field. For this gas density, even though the time-dependent collisional gas is overionized compared with CIE, the addition of photoionization by the metagalactic background increases the ionization states of the dominant coolants above and beyond those in the non-equilibrium collisional gas.

Figure 3 compares the TDP cooling efficiencies computed here to those of Oppenheimer & Schaye (2013, hereafter OS13). For a direct comparison, the figure shows the *net* cooling efficiencies, defined here as $\Lambda_{\text{net}} \equiv (n_{\text{H}}\Lambda_{\text{e,H}} - \Upsilon)/n_{\text{H}}$. OS13 provide online results for densities in the range $n_{\text{H}} = 10^{-5} \text{ cm}^{-3}$ and 10^{-2} cm^{-3} , which are displayed in Figure 3. Note, that these densities are all “high densities” (i.e. above the threshold density) in the context of the discussion that follows. I display results for solar metallicity gas exposed to the $z = 0$ HM12 radiation field. Figure 3 shows a very nice agreement between the results of this work (dashed curves) and OS13 (solid curves). The small differences seen between 10^5 K and $\sim 2 \times 10^6 \text{ K}$ have already been described in OS13, and are mainly due to differences in the solar composition assumed (see figure 5 and associated discussion in OS13). The low temperatures differences are all basically at thermal equilibrium, where cooling and heating become comparable, and the differences between them are minute. These results are also very sensitive to the high-energy cutoff of the input SED (see discussion in Appendix B). Overall, the agreement between the computed TDP cooling efficiencies presented in Figure 3, is better than the one presented in OS13 for the TDC rates, mainly due to the use of the more up-to-date atomic data included in the newer version of Cloudy (ver. 13.00).

The photoionization-equilibrium and non-equilibrium cooling efficiencies for the full parameter space considered in this work are presented in Tables 4 and 5, respectively. Full electronic tables are divided into lettered sections A–BC, as described in Table 3. Each lettered

section lists the cooling efficiencies as a function of temperature for the five metallicity values considered. The results are displayed in Figures 4–9.

Focus first on the results for $z = 0$, displayed in Figure 4. This figure shows the time-dependent cooling efficiencies as functions of temperature in gas photoionized by the $z = 0$ HM12 metagalactic radiation field, for gas metallicities Z equal to 2, 1, 10^{-1} , 10^{-2} and 10^{-3} times Z_{\odot} (top to bottom rows), and for gas densities between 10^3 and 10^{-7} cm^{-3} (shown by different colors within each row).

The non-equilibrium cooling efficiencies for “high” gas densities, $n \gtrsim 10^{-4} \text{ cm}^{-3}$, are displayed in the left hand side panels. The left panels also show the TDC (i.e. no radiation) non-equilibrium cooling efficiency in the gray solid curve shown in the background (GS07). The TDC cooling efficiency ($\text{erg s}^{-1} \text{ cm}^{-3}$) is independent of gas density.

In the TDC case — shown by the thick gray curve — cooling is dominated by metal-line emission over a wide range of temperatures for metallicities above $10^{-2} Z_{\odot}$ (three upper panels). For lower metallicities ($Z \lesssim 10^{-2} Z_{\odot}$, two lower panels), hydrogen and helium lines, which are suppressed by metal line cooling at higher- Z , dominate. At the highest temperatures, thermal bremsstrahlung emission dominates the energy losses. The transition between line-emission and bremsstrahlung occurs at a few $\times 10^7 \text{ K}$ for solar metallicity gas, and at $\sim 10^6 \text{ K}$ for the primordial case.

Figure 4 shows that the various time-dependent photoionized (hereafter TDP, see Table 2) cooling curves overlap with the TDC curve for high densities, where the ionization parameter is low, and the impact of photoionization therefore remains limited: the solid blue, dashed red, and thick gray curves overlap. For densities $\gtrsim 1 \text{ cm}^{-3}$, the TDP cooling efficiencies are identical to the TDC cooling efficiencies for all gas metallicities.

Below this density, a metallicity dependence emerges. For solar (or higher) metallicity, the TDP cooling efficiencies overlaps with the TDC cooling down to densities of $\sim 10^{-3} \text{ cm}^{-3}$, as is shown by the upper two panels. At lower metallicities ($Z \lesssim 0.1$), the cooling efficiencies in 10^{-3} cm^{-3} gas overlap with the collisional curve only for $T \gtrsim 2 \times 10^4 \text{ K}$. Below this temperature, cooling is suppressed, as the abundance of neutral hydrogen is reduced by the photoionizing radiation, leading to less efficient $\text{Ly}\alpha$ cooling. This does not affect higher-metallicity gas, because for $Z \gtrsim 1$ hydrogen remain almost completely ionized down to 10^4 K even with no photoionization. Metal emission lines then dominate the cooling down to 10^4 K .

For even lower densities $n \leq 10^{-4} \text{ cm}^{-3}$ the photoion-

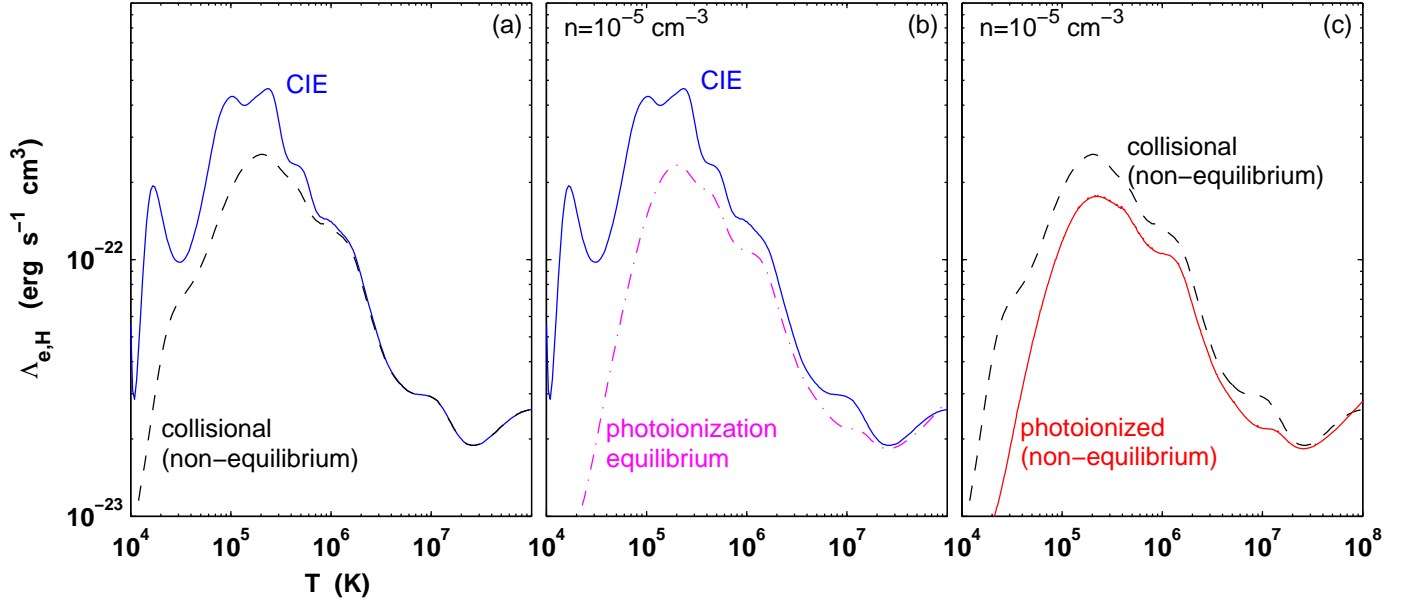


FIG. 2.— Cooling efficiencies ($\text{erg s}^{-1} \text{cm}^3$) versus temperature. (a) CIE cooling (solid blue) versus time-dependent collisional cooling (dashed black). Data from GS07. (b) CIE cooling (solid blue) versus PIE cooling (dash-dotted magenta curve) assuming a density of 10^{-5}cm^{-3} , and the $z = 0$ HM12 background; (c) TDC cooling (no radiation, dashed black) versus time-dependent cooling in photoionized gas with a density of 10^{-5}cm^{-3} (solid red).

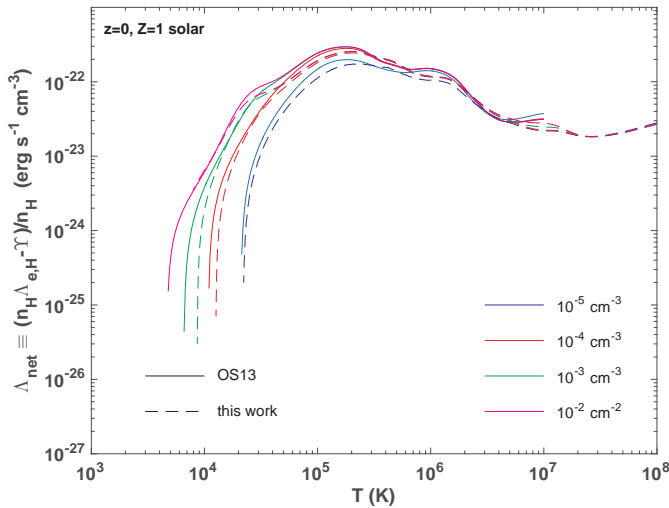


FIG. 3.— Net cooling efficiencies ($\equiv (n_H \Lambda_{e,H} - \Upsilon) / n_H \text{erg s}^{-1} \text{cm}^{-3}$) versus temperature in this work (dashed curves) versus OS13 for solar metallicity gas exposed to the $z =$ radiation field. The different colors correspond to different gas densities.

izing radiation modifies the ion fractions of the dominant metal coolants, and TDP cooling curves start to deviate from the collisional curve. For example, for $n = 10^{-4} \text{cm}^{-3}$ and $Z = 1 Z_\odot$ the TDP cooling efficiencies overlap with the TDC case for $T \gtrsim 5 \times 10^4 \text{K}$, whereas for $Z = 10^{-3} Z_\odot$ the curves overlap only for $T \gtrsim 2 \times 10^5 \text{K}$.

The cooling efficiencies for “low” gas densities, $\lesssim 10^{-4} \text{cm}^{-3}$, are shown in the right hand side panels. Again, the different rows are for different gas metallicities from $2 Z_\odot$ (top panel) to $10^{-3} Z_\odot$ (bottom panel). In each panel, the colored curves show the TDP cooling efficiencies at different gas densities. Here, the thick gray curves in the background show the cooling efficiencies as-

suming *photoionization equilibrium* with the background radiation. The PIE results *do* depend on the gas density, and there is a series of gray curves for the different densities displayed. The colored curves end at various temperatures, corresponding to the thermal equilibrium temperatures at the various densities.

For densities $\gtrsim 10^{-5} \text{cm}^{-3}$, the cooling is dominated by line emission at lower temperatures, and by thermal bremsstrahlung emission at the higher temperatures, just as for the higher densities displayed in the left hand side panels. However, at the lowest densities ($n \lesssim 10^{-6} \text{cm}^{-3}$) an additional cooling process comes into play, namely Compton cooling off the metagalactic background radiation. Compton cooling gives rise to the sharp increase in $\Lambda_{e,H}$ at high temperatures. The cooling efficiency becomes significantly higher than the thermal bremsstrahlung efficiency. Because Compton cooling is proportional to the electron density times photon density (see equation 1), as opposed to all other cooling processes which are proportional to the electron density squared, it dominates at low densities, where all other processes are suppressed. Note that because Λ is defined as the cooling rate per volume divided by $n_e n_H$, the compton cooling efficiency, $\Lambda_{e,H}^{\text{compton}} \propto n_H^{-1}$.

The right-hand-side panels show that for $n \leq 10^{-6}$ the TDP cooling curves overlap with the PIE curves for all gas metallicities. At higher gas densities departures from photoionization equilibrium occur. For example, for $n = 10^{-5} \text{cm}^{-3}$ the TDP cooling curves are identical to those in PIE for $Z < 1 Z_\odot$, whereas for $Z \geq 1 Z_\odot$, slight deviations between the TDP curves and the PIE curves are apparent near the peak of the cooling curve, $\sim 2 \times 10^5 \text{K}$.

An important conclusion from Figure 4 is that for every metallicity there exists a threshold density (or, equivalently, a threshold ionization parameter) below which the

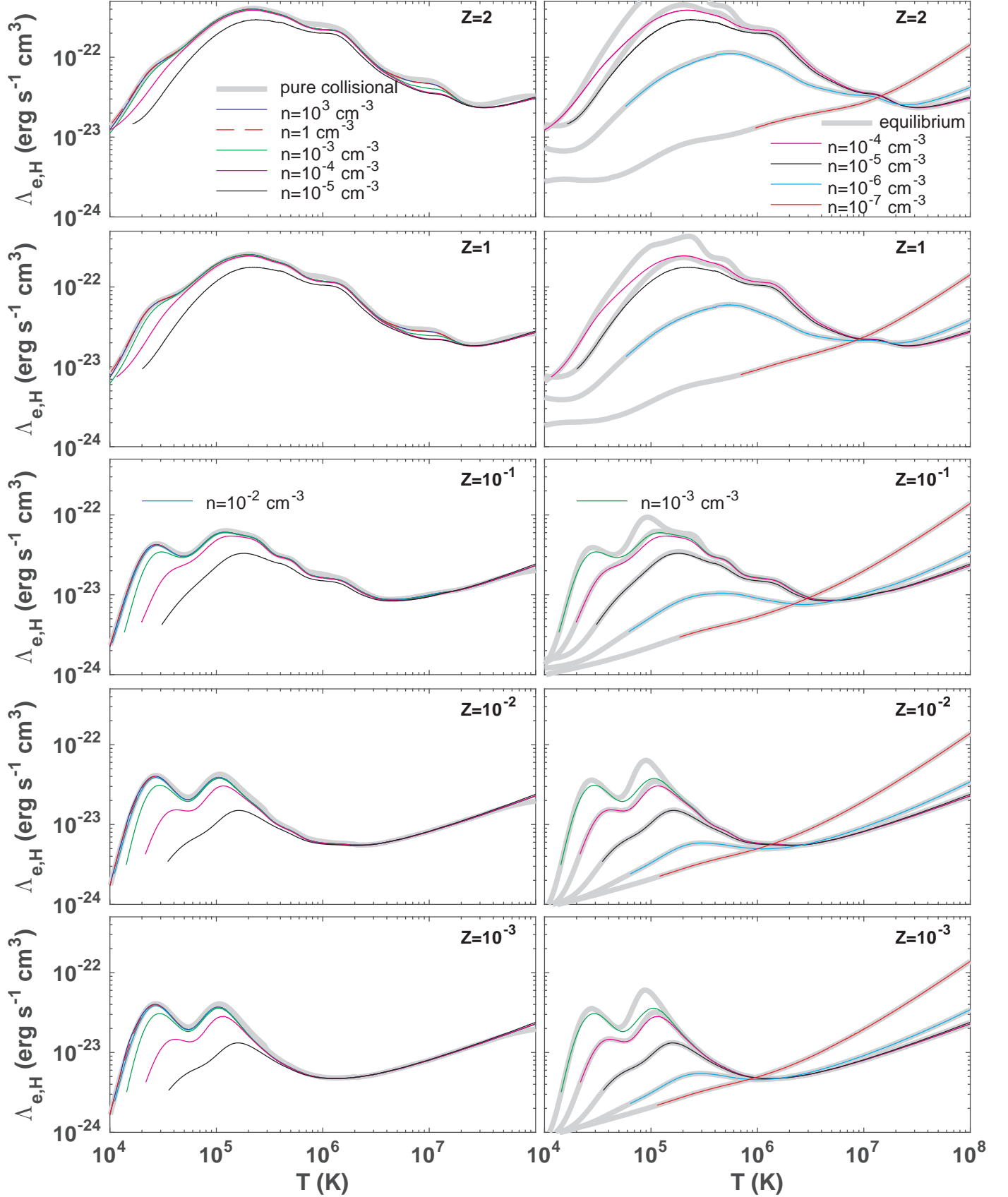


FIG. 4.— Time-dependent cooling efficiencies as functions of temperature in gas photoionized by the $z = 0$ metagalactic radiation field, for gas densities between 10^3 and 10^{-7} cm^{-3} (shown by different colors), and gas metallicities between 2 and 10^{-3} times solar (top to bottom panels). The colored curves end at the thermal equilibrium temperatures. For higher density gas, $\gtrsim 10^{-4} \text{ cm}^{-3}$ (shown in the left panels), the cooling efficiencies are similar to those in collisional gas with no external radiation. The time-dependent collisional cooling efficiency is independent of density, and is shown by the thick gray curve in the background. For lower densities, $\lesssim 10^{-4} \text{ cm}^{-3}$ (shown in the right panels), the cooling efficiencies are similar to those of gas in photoionization *equilibrium*, shown by the series of gray curves behind the colored curves.

TABLE 3
COOLING DATA GUIDE

Density (cm^{-3})	redshift	Lettered Index
10^{-7}	3	A
10^{-7}	2	B
10^{-7}	1	C
10^{-7}	0.5	D
10^{-7}	0	E
10^{-6}	3	F
10^{-6}	2	G
10^{-6}	1	H
10^{-6}	0.5	I
10^{-6}	0	J
10^{-5}	3	K
10^{-5}	2	L
10^{-5}	1	M
10^{-5}	0.5	N
10^{-5}	0	O
10^{-4}	3	P
10^{-4}	2	Q
10^{-4}	1	R
10^{-4}	0.5	S
10^{-4}	0	T
10^{-3}	3	U
10^{-3}	2	V
10^{-3}	1	W
10^{-3}	0.5	X
10^{-3}	0	Y
10^{-2}	3	Z
10^{-2}	2	AA
10^{-2}	1	AB
10^{-2}	0.5	AC
10^{-2}	0	AD
10^{-1}	3	AE
10^{-1}	2	AF
10^{-1}	1	AG
10^{-1}	0.5	AH
10^{-1}	0	AI
1	3	AJ
1	2	AK
1	1	AL
1	0.5	AM
1	0	AN
10^1	3	AO
10^1	2	AP
10^1	1	AQ
10^1	0.5	AR
10^1	0	AS
10^2	3	AT
10^2	2	AU
10^2	1	AV
10^2	0.5	AW
10^2	0	AX
10^3	3	AY
10^3	2	AZ
10^3	1	BA
10^3	0.5	BB
10^3	0	BC

NOTE. — A density-redshift index to lettered parts A–BC used in Tables 4–5, and 7–8.

cooling efficiencies are close to those in PIE, and above which they resemble those in TDC cooling gas with no external radiation. Above the threshold density, departures from equilibrium ionization are significant, but the impact of the photoionizing radiation may be neglected. Below this critical density, photoionization plays a significant role, but departures from equilibrium may be

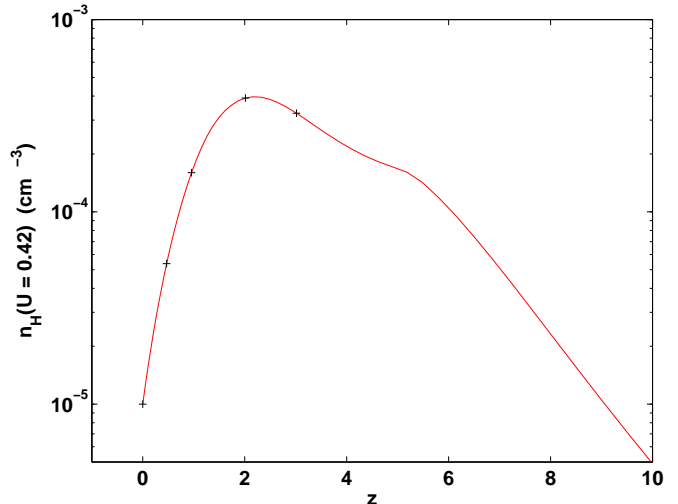


FIG. 5.— Density for which $U = 0.42$ as a function of redshift for the metagalactic radiation field (Haardt & Madau 2012). This is the density which marks the transition from *collisional* time-dependent cooling efficiencies to photoionization *equilibrium* cooling efficiencies in solar metallicity gas ($Z \sim 1$). In primordial gas, this transition occurs at densities which are a factor ~ 100 higher.

neglected.

For example, for $Z = 2 Z_{\odot}$ (top panels), the cooling efficiencies for $n > 10^{-5} \text{ cm}^{-3}$ overlap with the TDC cooling efficiency, whereas for $n < 10^{-5} \text{ cm}^{-3}$ the cooling curves overlap with the PIE curves. The threshold density, $n_{\text{th}}(Z = 2, z = 0) = 10^{-5} \text{ cm}^{-3}$, corresponds to an ionization parameter $U_{\text{th}} = 0.42$. For $Z = 10^{-3} Z_{\odot}$ (bottom panels) the TDP cooling efficiencies for $n > 10^{-3} \text{ cm}^{-3}$ overlap with the TDC cooling efficiency, whereas for $n < 10^{-3} \text{ cm}^{-3}$ the TDP cooling overlaps with the PIE curves. The threshold density, $n_{\text{th}}(Z = 10^{-3}, z = 0) = 10^{-3} \text{ cm}^{-3}$, corresponds to an ionization parameter $U_{\text{th}} = 4.2 \times 10^{-3}$. The threshold densities/ionization parameters for $z = 0$ are listed in table 6.

This finding offers a great computational simplification: instead of following the time dependent cooling efficiencies in the presence of photoionizing radiation, it is possible to use pre-computed tables for the TDC cooling efficiency (i.e. GS07) and/or for PIE.

Within $\sim a$ dex around the threshold ionization parameter, both departures from equilibrium ionization and photoionization affect the cooling efficiencies. However, even in this case it is enough to know the TDC and PIE cooling efficiencies: The TDP cooling efficiency deviates from the *minimum* of the TDC and PIE efficiencies by at most 20% (30%) for $Z \lesssim 0.1 Z_{\odot}$ ($\gtrsim 1 Z_{\odot}$) (for $z = 0$).

The cooling efficiencies for redshifts 0.5, 1, 2, and 3 are displayed in Figures 6–9, and listed in Tables 4 and 5. As in Figure 4, different rows are for different gas metallicities, and the different curves within each row represent different gas densities. “High” densities are on the left-hand side panels, and “low” densities are on the right hand side panels. Figures 6–9 confirm that for $z = 0.5 - 3$ there also exists a threshold density above which the TDP cooling is similar to the TDC curve and below which it is similar to that in PIE.

Figure 4 shows that the threshold ionization parameter corresponding to $Z \gtrsim 1 Z_{\odot}$ is $U = 0.42$. For $z = 0$,

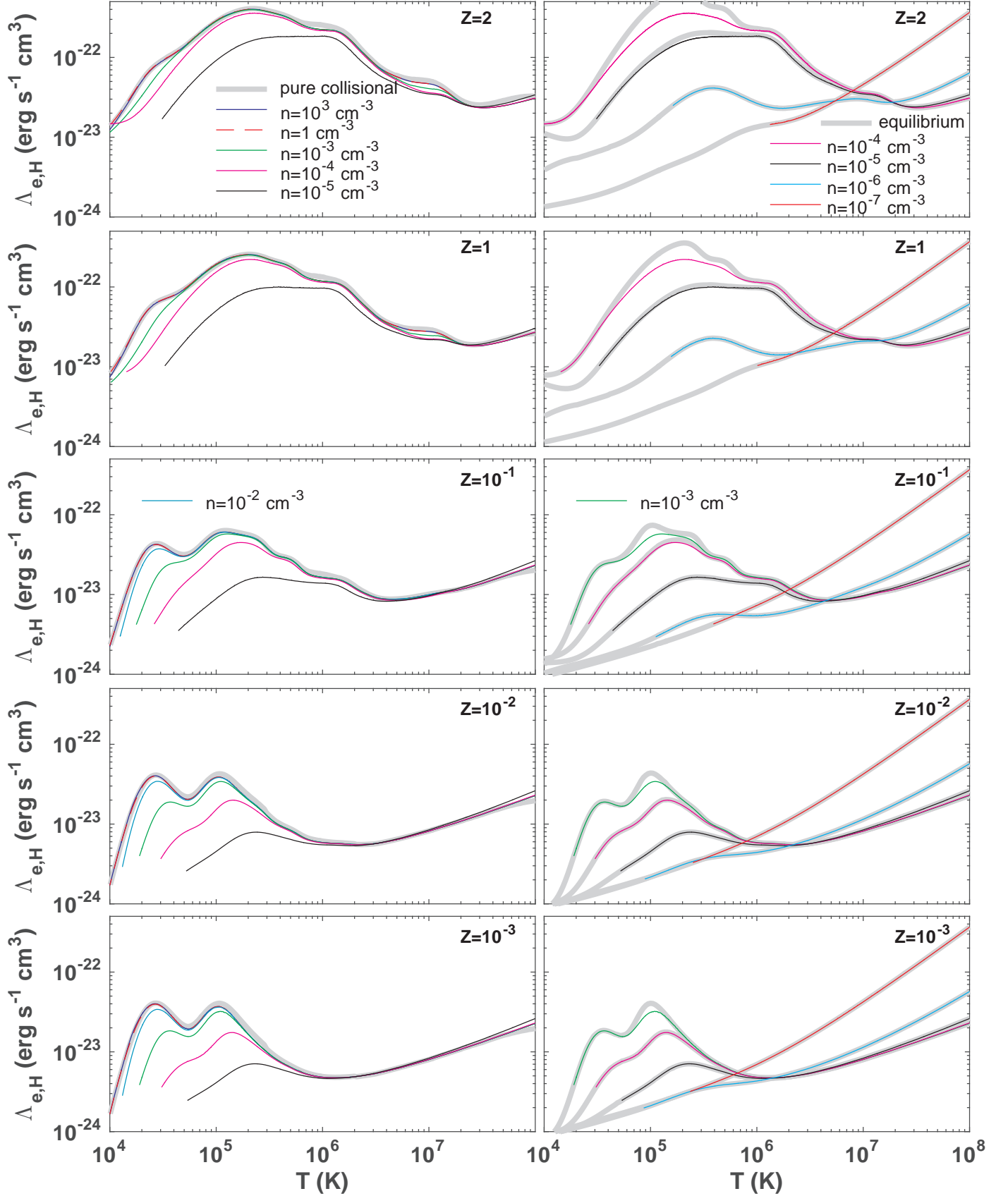


FIG. 6.— Same as Figure 4, but for the metagalactic radiation field at $z = 0.5$.

TABLE 4
EQUILIBRIUM COOLING EFFICIENCIES (ERG S⁻¹ CM³)

Temperature (K)	$\Lambda_{e,H}(Z = 10^{-3})$	$\Lambda_{e,H}(Z = 10^{-2})$	$\Lambda_{e,H}(Z = 10^{-1})$	$\Lambda_{e,H}(Z = 1)$	$\Lambda_{e,H}(Z = 2)$
1.0000×10^8	1.24×10^{21}	1.24×10^{21}	1.24×10^{21}	1.24×10^{21}	1.23×10^{21}
9.5012×10^7	1.18×10^{21}	1.18×10^{21}	1.18×10^{21}	1.18×10^{21}	1.17×10^{21}
9.0273×10^7	1.12×10^{21}	1.12×10^{21}	1.13×10^{21}	1.12×10^{21}	1.11×10^{21}
8.5770×10^7	1.07×10^{21}	1.07×10^{21}	1.08×10^{21}	1.07×10^{21}	1.06×10^{21}
\vdots	\vdots	\vdots	\vdots	\vdots	\vdots

NOTE. — The complete version of this table is in the electronic edition of the Journal. The printed edition contains only a sample. The full table is divided into lettered parts A–BC, and lists the equilibrium cooling efficiencies for for gas densities between 10^{-7} and 10^3 cm⁻³, for the metagalactic backgrounds at redshifts 0–3, and for $Z = 10^{-3}$, 10^{-2} , 10^{-1} , 1, and 2 times solar metallicity gas (for a guide, see Table 3).

TABLE 5
NON-EQUILIBRIUM COOLING EFFICIENCIES (ERG S⁻¹ CM³)

Temperature (K)	$\Lambda_{e,H}(Z = 10^{-3})$	$\Lambda_{e,H}(Z = 10^{-2})$	$\Lambda_{e,H}(Z = 10^{-1})$	$\Lambda_{e,H}(Z = 1)$	$\Lambda_{e,H}(Z = 2)$
$1.0000 \times 10^{+8}$	1.24×10^{-21}	1.24×10^{-21}	1.24×10^{-21}	1.24×10^{-21}	1.23×10^{-21}
$9.9000 \times 10^{+7}$	1.23×10^{-21}	1.23×10^{-21}	1.23×10^{-21}	1.23×10^{-21}	1.22×10^{-21}
$9.8010 \times 10^{+7}$	1.22×10^{-21}	1.22×10^{-21}	1.22×10^{-21}	1.22×10^{-21}	1.20×10^{-21}
$9.7030 \times 10^{+7}$	1.20×10^{-21}	1.20×10^{-21}	1.20×10^{-21}	1.21×10^{-21}	1.19×10^{-21}
\vdots	\vdots	\vdots	\vdots	\vdots	\vdots

NOTE. — The complete version of this table is in the electronic edition of the Journal. The printed edition contains only a sample. The full table is divided into lettered parts A–BC, and lists the non-equilibrium cooling efficiencies for for gas densities between 10^{-7} and 10^3 cm⁻³, for the metagalactic backgrounds at redshifts 0–3, and for $Z = 10^{-3}$, 10^{-2} , 10^{-1} , 1, and 2 times solar metallicity gas (for a guide, see Table 3).

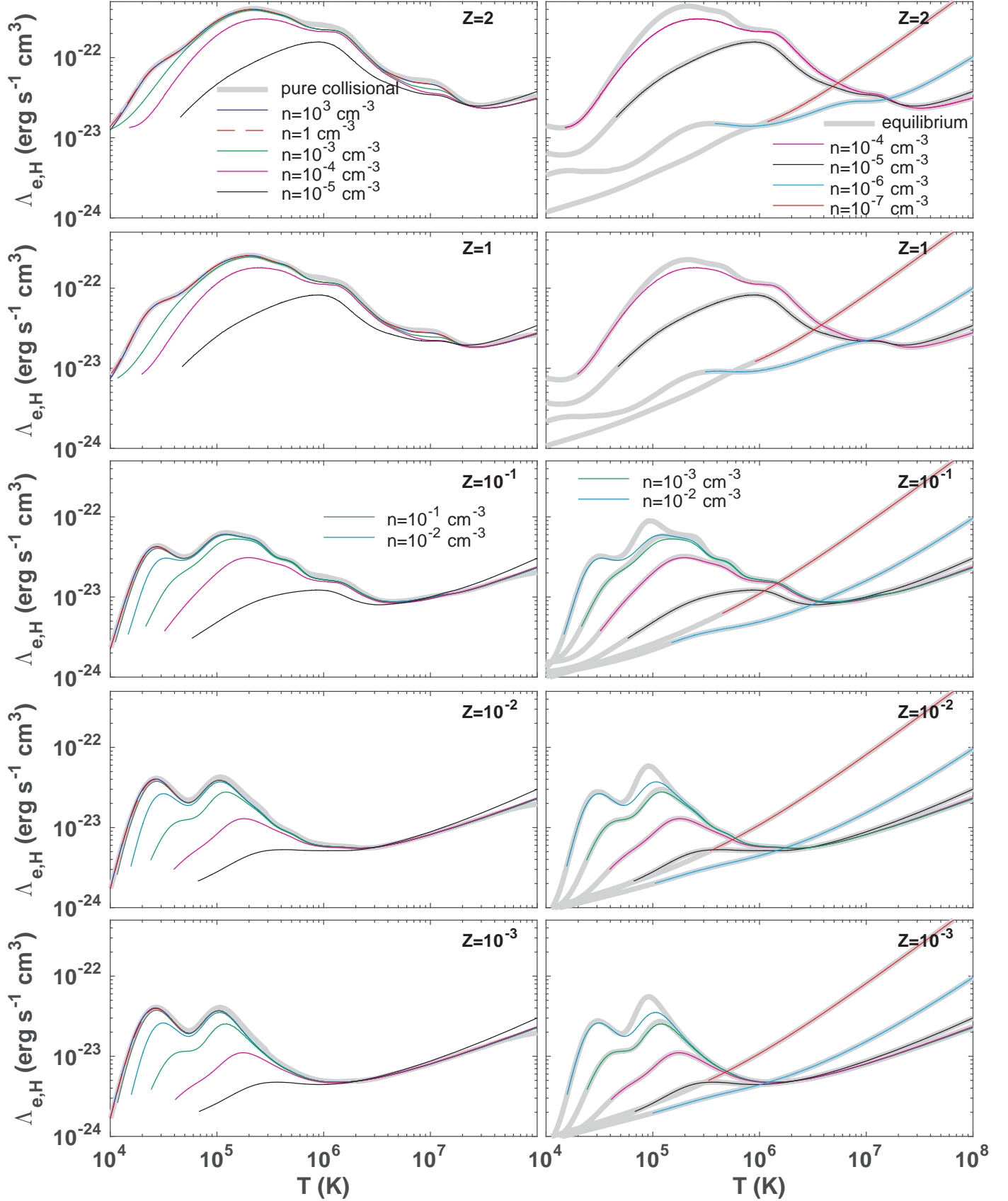


FIG. 7.— Same as Figure 4, but for the metagalactic radiation field at $z = 1$.

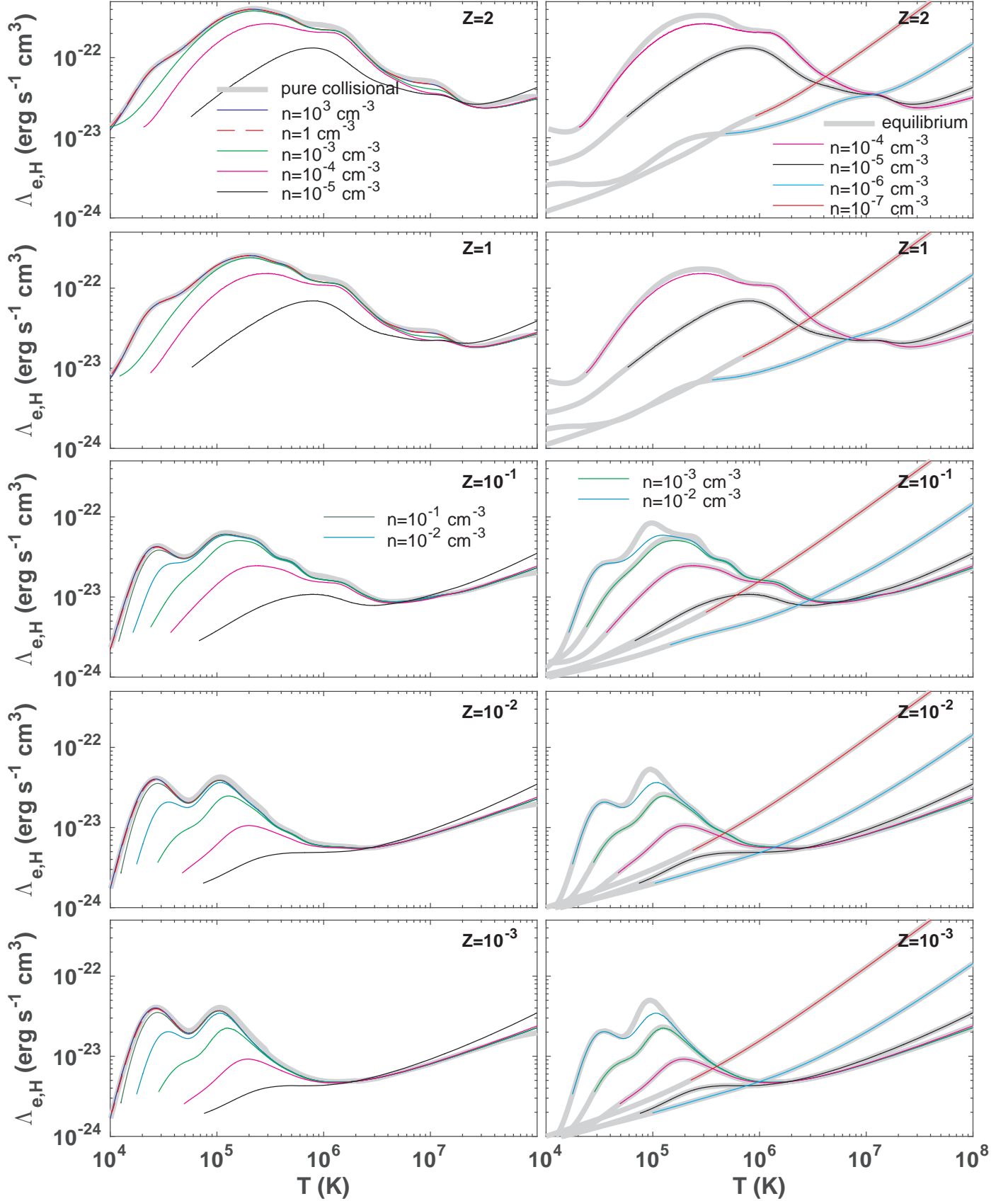


FIG. 8.— Same as Figure 4, but for the metagalactic radiation field at $z = 2$.

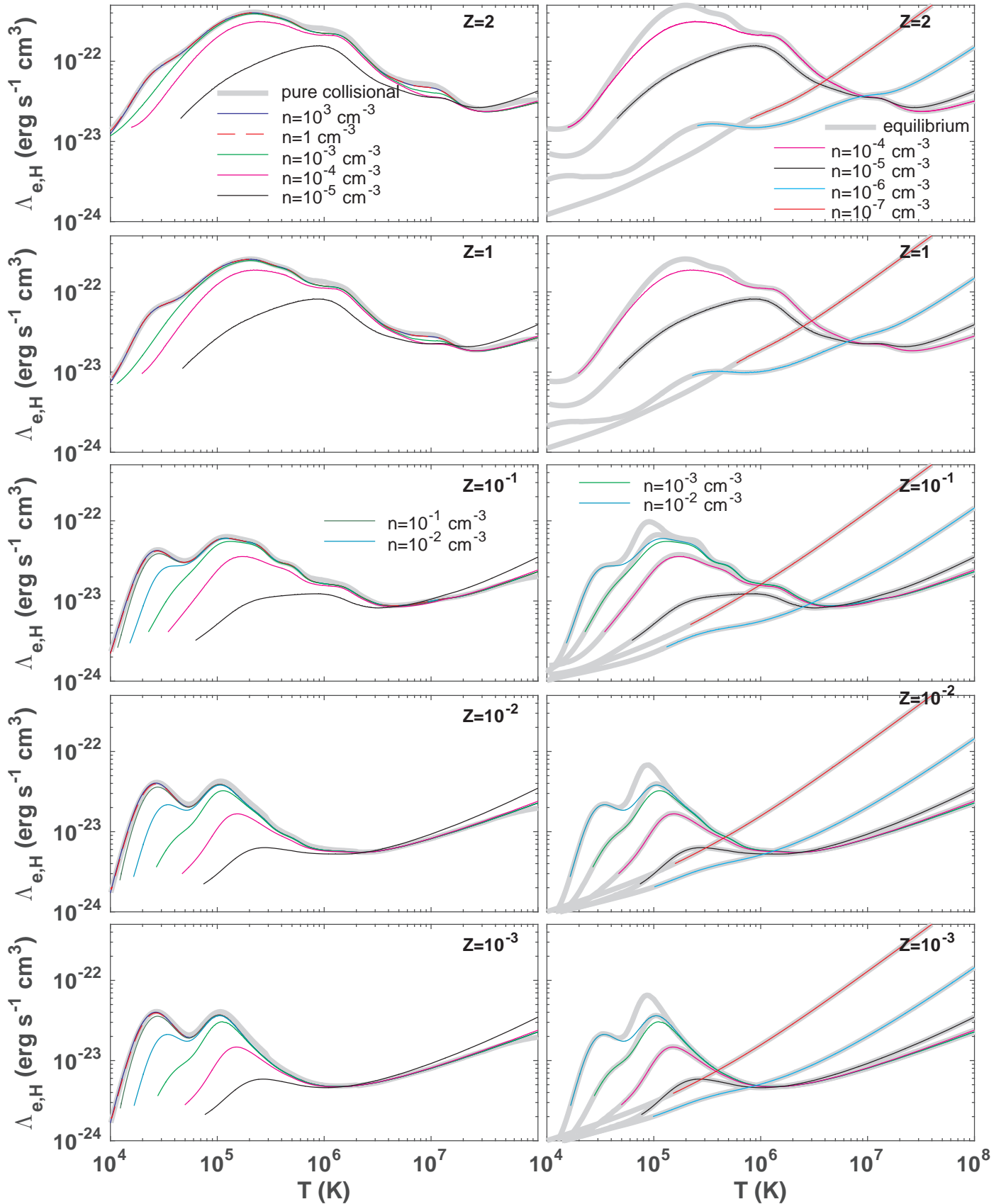


FIG. 9.— Same as Figure 4, but for the metagalactic radiation field at $z = 3$.

TABLE 6
THRESHOLD IONIZATION PARAMETERS

Metallicity (Z_{\odot})	$n_{\text{th}}(z=0)$ (cm^{-3})	U_{th}
1 – 2	10^{-5}	4.2×10^{-1}
$10^{-1} - 10^{-3}$	10^{-3}	4.2×10^{-3}

this corresponds to a critical density of 10^{-5} cm^{-3} . For higher redshifts, the density corresponding to this ionization parameter is modified as the spectral energy distribution of the metagalactic background evolves. The threshold densities corresponding to the threshold ionization parameter, $U = 0.42$ are displayed in Figure 5. And indeed, Figures 6-9 verify that these threshold densities separate a high-density limit in which TDP cooling is equivalent to TDC cooling, from a low-density limit in which the TDP cooling is identical to that in PIE. For metallicities $\lesssim 10^{-1} Z_{\odot}$ the threshold ionization parameter is a factor of 100 lower than for solar metallicity ($U = 4.2 \times 10^{-3}$), and the threshold densities are therefore a factor of 100 higher than those displayed in Figure 5.

Heating in photoionized plasma is due to photoionization of atomic and ionic species. The heating rates therefore depend on the specific spectral energy distribution impinging upon the gas. The heating rates are coupled to the ionization states in the gas, which are affected by the same background. Over most of the temperature range considered here, heating is negligible with respect to cooling, and has little impact on the thermal evolution of the gas. Heating only modifies the thermal evolution near the thermal equilibrium temperature. For completeness, I list in Tables 7 and 8 the equilibrium and non-equilibrium heating rates for gas cooling in the presence of the metagalactic background radiation at redshifts, $z = 0, 0.5, 1, 2,$ and 3 (HM12). A guide is provided in Table 3. As mentioned before, throughout this paper, the Haardt & Madau (2012) background radiation has been truncated at an energy of $\sim 8,330 \text{ keV}$. While this high-energy truncation point has a negligible effect of the cooling efficiencies, which are the main focus of this paper, it plays a potentially important role in setting the absolute heating rates. Nevertheless, it is not expected to significantly affect the thermal evolution of low density plasmas. This point is further discussed in Appendix B.

3.1. Isobaric Cooling

Depending on the ratio between the cooling time and the dynamical time, cooling may proceed either isochorically (when cooling is rapid), or isobarically (when cooling is slow). The dynamical evolution is therefore determined by the ratio

$$\frac{t_c}{t_d} \propto \frac{T^{3/2}}{n\Delta D} \quad (6)$$

where $t_c \propto T/n/\Lambda$ is the cooling time, and $t_d \propto D/c_s \propto D/\sqrt{T}$ is the dynamical time in a gas cloud of size D , and sound speed c_s (see GS07 for a detailed discussion).

For isochoric cooling, D and n remain constant with

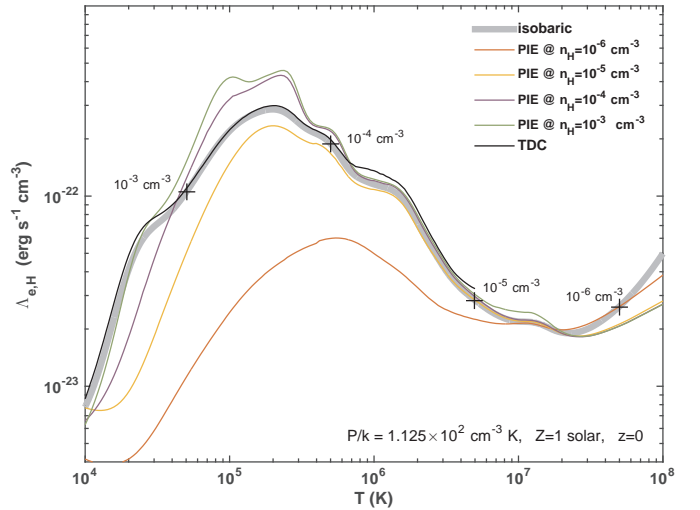


FIG. 10.— Isobaric cooling efficiency (thick gray) for gas exposed to the $z = 0$ metagalactic radiation field, for an assumed pressure of $112.5 \text{ cm}^{-3} \text{ K}$, and for solar abundances. The colored curves show the PIE cooling efficiencies for solar metallicity gas at densities between 10^{-6} and 10^{-3} cm^{-3} (red to green). The black curve shows the isobaric TDC cooling efficiency. The crosses and labels mark the hydrogen density at certain points along the cooling process. The time-dependent isobaric cooling matches the PIE cooling at the appropriate local density for densities below the threshold density, and the TDC cooling efficiency for densities greater than the threshold density.

time. As the gas cools, t_c/t_d generally decreases, implying that cooling which is initially isochoric remains isochoric. For isobaric cooling, the gas contracts as it cools. After cooling to a temperature T , the density will increase by a factor T_0/T , and the diameter will decrease by a factor $(T/T_0)^{1/3}$ relative to the properties at the initial temperature, T_0 . Thus, as the cloud cools and contracts, t_c/t_d decreases and a transition to isochoric cooling must eventually occur.

When the gas cools isobarically in the presence of photoionizing radiation the varying density also implies a varying ionization parameter. Consider the evolution of an isobarically cooling gas cloud. A gas cloud that begins the cooling process at a density larger than the threshold density, will always remain at a higher density. In this regime, one may consider the TDC cooling efficiency throughout the cooling process.

For a gas cloud that is initially at a density lower than the threshold density, cooling will initially proceed according to the PIE efficiencies. However, the density will increase by a factor (T_0/T) after cooling to a temperature T . The cloud may cross the threshold density, thus transitioning from the regime in which the PIE cooling efficiencies apply, into the regime where the TDC cooling efficiency apply.

This point is demonstrated in Figure 10. The thick gray curve depicts the time-dependent cooling efficiency in an *isobarically* cooling gas cloud with a constant pressure $P = 112.5 \text{ cm}^{-3} \text{ K}$, and solar metallicity, exposed to the $z = 0$ metagalactic radiation field. This gas begins its cooling process at an initial temperature $T_0 = 10^8 \text{ K}$, and density $n_{\text{H},0} = 5 \times 10^{-7} \text{ cm}^{-3}$, and achieves thermal

TABLE 7
EQUILIBRIUM HEATING RATES (ERG S⁻¹)

Temperature (K)	$\Upsilon_{\text{H}}(Z = 10^{-3})$	$\Upsilon_{\text{H}}(Z = 10^{-2})$	$\Upsilon_{\text{H}}(Z = 10^{-1})$	$\Upsilon_{\text{H}}(Z = 1)$	$\Upsilon_{\text{H}}(Z = 2)$
$1.0000 \times 10^{+8}$	3.13×10^{-31}	3.13×10^{-31}	3.15×10^{-31}	3.38×10^{-31}	3.63×10^{-31}
$9.5010 \times 10^{+7}$	3.13×10^{-31}	3.13×10^{-31}	3.15×10^{-31}	3.39×10^{-31}	3.65×10^{-31}
$9.0270 \times 10^{+7}$	3.13×10^{-31}	3.13×10^{-31}	3.19×10^{-31}	3.40×10^{-31}	3.67×10^{-31}
$8.5770 \times 10^{+7}$	3.13×10^{-31}	3.13×10^{-31}	3.19×10^{-31}	3.41×10^{-31}	3.70×10^{-31}
\vdots	\vdots	\vdots	\vdots	\vdots	\vdots

NOTE. — The complete version of this table is in the electronic edition of the Journal. The printed edition contains only a sample. The full table is divided into lettered parts A–BC, and lists the equilibrium heating rates for for gas densities between 10^{-7} and 10^3 cm⁻³, for the metagalactic backgrounds at redshifts 0–3, and for $Z = 10^{-3}$, 10^{-2} , 10^{-1} , 1, and 2 times solar metallicity gas (for a guide, see Table 3).

TABLE 8
NON-EQUILIBRIUM HEATING RATES (ERG S⁻¹)

Temperature (K)	$\Upsilon_{\text{H}}(Z = 10^{-3})$	$\Upsilon_{\text{H}}(Z = 10^{-2})$	$\Upsilon_{\text{H}}(Z = 10^{-1})$	$\Upsilon_{\text{H}}(Z = 1)$	$\Upsilon_{\text{H}}(Z = 2)$
$1.0000 \times 10^{+8}$	3.13×10^{-31}	3.13×10^{-31}	3.15×10^{-31}	3.37×10^{-31}	3.62×10^{-31}
$9.9000 \times 10^{+7}$	3.13×10^{-31}	3.13×10^{-31}	3.15×10^{-31}	3.38×10^{-31}	3.63×10^{-31}
$9.8010 \times 10^{+7}$	3.13×10^{-31}	3.13×10^{-31}	3.15×10^{-31}	3.38×10^{-31}	3.64×10^{-31}
$9.7030 \times 10^{+7}$	3.13×10^{-31}	3.13×10^{-31}	3.15×10^{-31}	3.39×10^{-31}	3.64×10^{-31}
\vdots	\vdots	\vdots	\vdots	\vdots	\vdots

NOTE. — The complete version of this table is in the electronic edition of the Journal. The printed edition contains only a sample. The full table is divided into lettered parts A–BC, and lists the non-equilibrium heating rates for for gas densities between 10^{-7} and 10^3 cm⁻³, for the metagalactic backgrounds at redshifts 0–3, and for $Z = 10^{-3}$, 10^{-2} , 10^{-1} , 1, and 2 times solar metallicity gas (for a guide, see Table 3).

equilibrium at a temperature $T_{\text{eq}} = 1.13 \times 10^4$ K, when its density is $n_{\text{eq}} = 4.8 \times 10^{-3}$ cm⁻³. The crosses and labels mark the hydrogen density at certain points along the cooling process.

The colored curves displayed in Figure 10 show the PIE cooling efficiencies at densities of $10^{-6} - 10^{-3}$ cm⁻³ (from red to green). The black curve shows the (isobaric) TDC cooling efficiency (GS07). The cooling efficiency is indeed identical to the PIE cooling efficiency at the appropriate density, as long as the gas density is lower than the threshold density. For example, the isobaric thick gray curve and the PIE red curve intersect just when the density equals 10^{-6} cm⁻³ (marked by the cross). The isobaric curve crosses the orange curve when the density equals 10^{-5} cm⁻³, as expected. At $\sim 10^{-5}$ cm⁻³ the gas crosses the threshold density, and at lower temperatures (higher densities) we therefore expect the cooling efficiency to match the TDC cooling efficiency. And indeed, at lower temperature, the isobaric gray curve matches the TDC black curve, and not the (purple, green) PIE curves.

Figure 10 demonstrates that the threshold density can be used to separate the regime in which PIE cooling efficiencies apply from the regime in which the cooling efficiency is the TDC efficiency, even for the case of isobaric cooling.

4. ION FRACTIONS

I have carried out computations of the photoionized ion fractions of the elements H, He, C, N, O, Ne, Mg, Si,

S, and Fe, as functions of gas temperature for two sets of assumptions. First I assume PIE imposed at all T. Then I consider the nonequilibrium ion fractions in TDP gas as a function of the time-dependent temperature. The results are listed in tabular form in Tables 10 and 11 for the PIE and TDP ion fractions, respectively. These tables are divided into numbered parts 1–275, as described in Table 9.

In §3, I introduced the threshold ionization parameter, which separates the regime in which radiation significantly affects the cooling efficiencies (but departures from equilibrium may be neglected), from the regime in which non-equilibrium effects become important (but radiation may be neglected). Here I consider the corresponding behavior of the ion fractions for different gas densities.

For solar metallicity gas exposed to the $z = 0$ metagalactic background, the threshold ionization parameter corresponds to a threshold hydrogen density $n_{\text{H}} = 10^{-5}$ cm⁻³. Figure 11 presents the evolution of some ion fractions for this threshold gas density (for $Z = 1Z_{\odot}$, and the $z = 0$ metagalactic background). This is the density for which the impact of time-dependent photoionization should be maximal. In Figure 11, the dark curves present the results for the TDP ion fractions. This is compared to the ion fractions in PIE (thick gray curves), as well as to the ion fractions in TDC cooling gas (thin gray curves). The top panels display the ion fractions of hydrogen (left) and helium (right) as functions of temperature, and the bottom panel is for carbon. The different

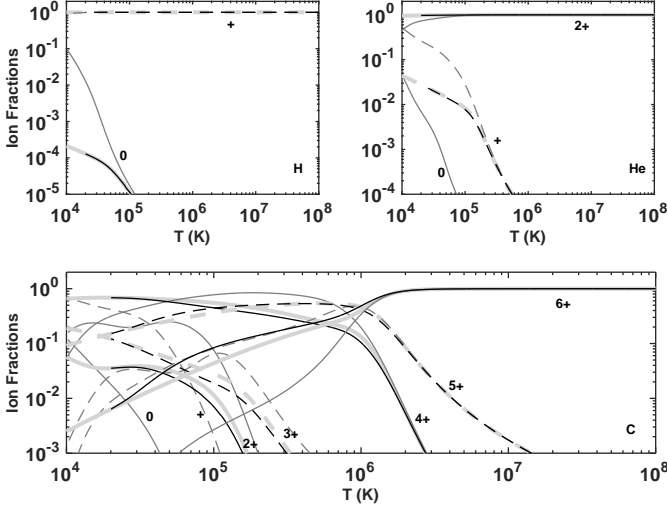


FIG. 11.— Ion fractions $x_i n_{i,m}/n_H A_m$, vs. gas temperature, for $n_H = 10^{-5} \text{ cm}^{-3}$, solar metallicity gas exposed to the $z = 0$ metagalactic radiation. The TDP ion fractions are displayed by the dark curves, the PIE ion fractions are in thick gray curves, and the TDC ion fractions are in the thin gray curves. The different ionization states are shown by the dashed and solid curves (alternately; Neutrals are in solid, singly ionized dashed, etc.) and are labeled in each panel. The top panels are for hydrogen (left), and helium (right) and the bottom panel is for carbon.

ionization states in each panel are denoted by dashed and solid curves (alternately), and are labeled next to the curves.

Figure 11 shows that for this density gas in PIE (thick gray) is more highly ionized than gas overionized due to time-dependent cooling in the absence of external radiation (TDC, thin gray). Moreover, TDP cooling leads to recombination lags which cause the gas to be ionized above and beyond the ionization in PIE. For example, at a temperature of $3 \times 10^5 \text{ K}$, the C^{3+} , C^{4+} , C^{5+} , and C^{6+} fractions are 3.9×10^{-3} , 8.0×10^{-1} , 1.8×10^{-1} , and 1.3×10^{-2} in TDC gas, 1.6×10^3 , 3.6×10^{-1} , 5.1×10^{-1} , and 1.3×10^{-1} for PIE, and 1.2×10^{-3} , 2.9×10^{-1} , 5.3×10^{-1} , and 1.8×10^1 in TDP cooling gas. As far as the ionization states are concerned, the threshold density represents a case for which the ion fractions significantly deviate (by factors up to 4) from both PIE and TDC ion fractions. This is in contrast to the cooling efficiencies which deviate from the *minimum* of the TDC and PIE efficiencies by at most 20 – 30% (see Section 3).

Figure 12 displays the ion fractions for gas 2 dex above the threshold density, $n_H = 10^{-3} \text{ cm}^{-3}$. For this density, the TDP cooling efficiencies are identical to the TDC cooling efficiencies for all temperatures above $4 \times 10^4 \text{ K}$, and even at for lower temperatures the differences remain limited. However, the abundance of certain species (e.g. Si^{5+}) are more strongly affected by the recombination lags in the photoionized cooling gas, and may differ significantly (by factors up to ~ 4) from those of the TDC cooling gas even at higher temperatures.

Figure 13 considers a hydrogen density of 10^{-7} cm^{-3} , 2 dex below the threshold density. In this case, the cooling gas reaches thermal equilibrium at a temperature $\sim 7 \times 10^5 \text{ K}$. Throughout the cooling process, all ion fractions are identical (to within a few %) to those in PIE.

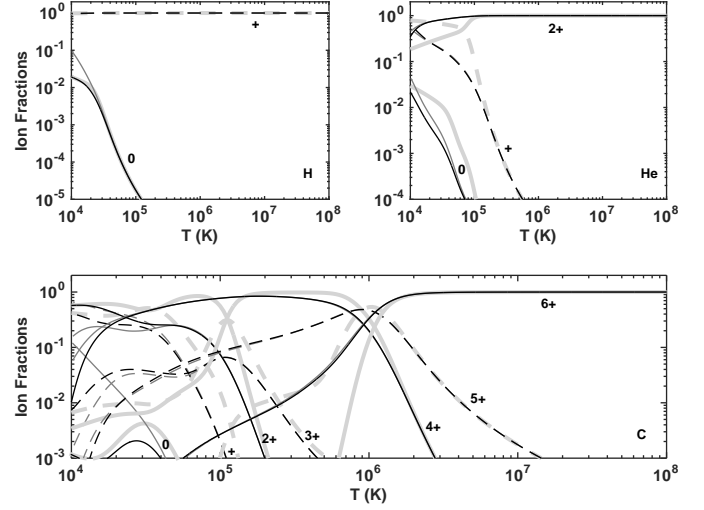


FIG. 12 — Same as Figure 12 but for $n_H = 10^{-3} \text{ cm}^{-3}$

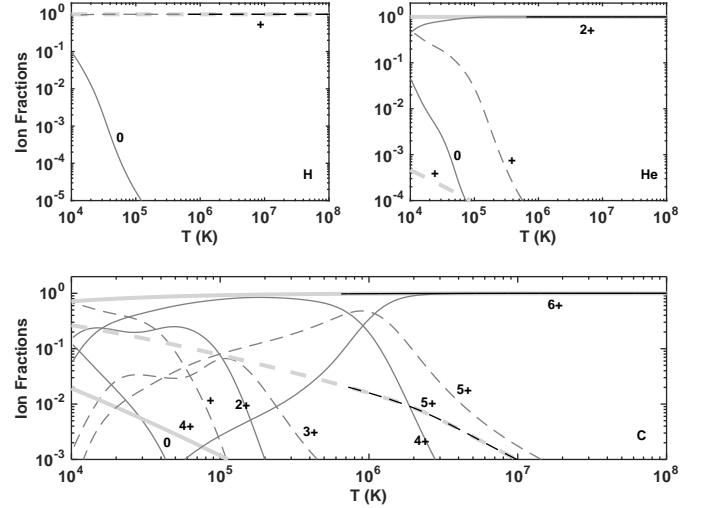


FIG. 13.— Same as Figure 12, but for $n_H = 10^{-7} \text{ cm}^{-3}$

Figures 14-17 display the ratio between the TDP ion fractions and the TDC ion fractions (top panels) of the dominant coolants C^{3+} , N^{4+} , O^{5+} , and Ne^{7+} (for clarity, data is only presented when the absolute abundance in the TDP gas is $> 10^{-3}$). The ratios for different gas densities are displayed by different curves. As expected, the TDP/TDC ion fraction of these species is \sim unity for all gas densities $\gtrsim 10^{-4} \text{ cm}^{-3}$, except at $T \lesssim 2 \times 10^4 \text{ K}$.

The bottom panels of Figures 14-17 display the ratio between the TDP ion fractions and the PIE ion fractions for the same species. These Figures demonstrate that the ion fraction ratio approaches unity for densities $\lesssim 10^{-5} \text{ cm}^{-3}$.

The convergence of the TDP ion abundance of the dominant coolants to the TDC abundances above the threshold density, and to the PIE abundances below the threshold density, confirm the results of section 3, and verify that the cooling efficiencies are only affected by both departures from equilibrium and photoionization at densities very close to the threshold density.

n_{H} (cm^{-3})	z	Z (Z_{\odot})	part	n_{H} (cm^{-3})	z	Z (Z_{\odot})	part	n_{H} (cm^{-3})	z	Z (Z_{\odot})	part	n_{H} (cm^{-3})	z	Z (Z_{\odot})	part	n_{H} (cm^{-3})	z	Z (Z_{\odot})	part
10 ⁻⁷	3	10 ⁻³	1	10 ⁻⁵	2	10 ⁻³	56	10 ⁻³	1	10 ⁻³	111	10 ⁻¹	0.5	10 ⁻³	166	10	0	10 ⁻³	221
10 ⁻⁷	3	10 ⁻²	2	10 ⁻⁵	2	10 ⁻²	57	10 ⁻³	1	10 ⁻²	112	10 ⁻¹	0.5	10 ⁻²	167	10	0	10 ⁻²	222
10 ⁻⁷	3	10 ⁻¹	3	10 ⁻⁵	2	10 ⁻¹	58	10 ⁻³	1	10 ⁻¹	113	10 ⁻¹	0.5	10 ¹	168	10	0	10 ⁻¹	223
10 ⁻⁷	3	1	4	10 ⁻⁵	2	1	59	10 ⁻³	1	1	114	10 ⁻¹	0.5	1	169	10	0	1	224
10 ⁻⁷	3	2	5	10 ⁻⁵	2	2	60	10 ⁻³	1	2	115	10 ⁻¹	0.5	2	170	10	0	2	225
10 ⁻⁷	2	10 ⁻³	6	10 ⁻⁵	1	10 ⁻³	61	10 ⁻³	0.5	10 ⁻³	116	10 ⁻¹	0	10 ⁻³	171	10 ²	3	10 ⁻³	226
10 ⁻⁷	2	10 ⁻²	7	10 ⁻⁵	1	10 ⁻²	62	10 ⁻³	0.5	10 ⁻²	117	10 ⁻¹	0	10 ⁻²	172	10 ²	3	10 ⁻²	227
10 ⁻⁷	2	10 ⁻¹	8	10 ⁻⁵	1	10 ⁻¹	63	10 ⁻³	0.5	10 ⁻¹	118	10 ⁻¹	0	10 ⁻¹	173	10 ²	3	10 ⁻¹	228
10 ⁻⁷	2	1	9	10 ⁻⁵	1	1	64	10 ⁻³	0.5	1	119	10 ⁻¹	0	1	174	10 ²	3	1	229
10 ⁻⁷	2	2	10	10 ⁻⁵	1	2	65	10 ⁻³	0.5	2	120	10 ⁻¹	0	2	175	10 ²	3	2	230
10 ⁻⁷	1	10 ⁻³	11	10 ⁻⁵	0.5	10 ⁻³	66	10 ⁻³	0	10 ⁻³	121	1	3	10 ⁻³	176	10 ²	2	10 ⁻³	231
10 ⁻⁷	1	10 ⁻²	12	10 ⁻⁵	0.5	10 ⁻²	67	10 ⁻³	0	10 ⁻²	122	1	3	10 ⁻²	177	10 ²	2	10 ⁻²	232
10 ⁻⁷	1	10 ⁻¹	13	10 ⁻⁵	0.5	10 ⁻¹	68	10 ⁻³	0	10 ⁻¹	123	1	3	10 ⁻¹	178	10 ²	2	10 ⁻¹	233
10 ⁻⁷	1	1	14	10 ⁻⁵	0.5	1	69	10 ⁻³	0	1	124	1	3	1	179	10 ²	2	1	234
10 ⁻⁷	1	2	15	10 ⁻⁵	0.5	2	70	10 ⁻³	0	2	125	1	3	2	180	10 ²	2	2	235
10 ⁻⁷	0.5	10 ⁻³	16	10 ⁻⁵	0	10 ⁻³	71	10 ⁻²	3	10 ⁻³	126	1	2	10 ⁻³	181	10 ²	1	10 ⁻³	236
10 ⁻⁷	0.5	10 ⁻²	17	10 ⁻⁵	0	10 ⁻²	72	10 ⁻²	3	10 ⁻²	127	1	2	10 ⁻²	182	10 ²	1	10 ⁻²	237
10 ⁻⁷	0.5	10 ⁻¹	18	10 ⁻⁵	0	10 ⁻¹	73	10 ⁻²	3	10 ⁻¹	128	1	2	10 ⁻¹	183	10 ²	1	10 ⁻¹	238
10 ⁻⁷	0.5	1	19	10 ⁻⁵	0	1	74	10 ⁻²	3	1	129	1	2	1	184	10 ²	1	1	239
10 ⁻⁷	0.5	2	20	10 ⁻⁵	0	2	75	10 ⁻²	3	2	130	1	2	2	185	10 ²	1	2	240
10 ⁻⁷	0	10 ⁻³	21	10 ⁻⁴	3	10 ⁻³	76	10 ⁻²	2	10 ⁻³	131	1	1	10 ⁻³	186	10 ²	0.5	10 ⁻³	241
10 ⁻⁷	0	10 ⁻²	22	10 ⁻⁴	3	10 ⁻²	77	10 ⁻²	2	10 ⁻²	132	1	1	10 ⁻²	187	10 ²	0.5	10 ⁻²	242
10 ⁻⁷	0	10 ⁻¹	23	10 ⁻⁴	3	10 ⁻¹	78	10 ⁻²	2	10 ⁻¹	133	1	1	10 ⁻¹	188	10 ²	0.5	10 ⁻¹	243
10 ⁻⁷	0	1	24	10 ⁻⁴	3	1	79	10 ⁻²	2	1	134	1	1	1	189	10 ²	0.5	1	244
10 ⁻⁷	0	2	25	10 ⁻⁴	3	2	80	10 ⁻²	2	2	135	1	1	2	190	10 ²	0.5	2	245
10 ⁻⁶	3	10 ⁻³	26	10 ⁻⁴	2	10 ⁻³	81	10 ⁻²	1	10 ⁻³	136	1	0.5	10 ⁻³	191	10 ²	0	10 ⁻³	246
10 ⁻⁶	3	10 ⁻²	27	10 ⁻⁴	2	10 ⁻²	82	10 ⁻²	1	10 ⁻²	137	1	0.5	10 ⁻²	192	10 ²	0	10 ⁻²	247
10 ⁻⁶	3	10 ⁻¹	28	10 ⁻⁴	2	10 ⁻¹	83	10 ⁻²	1	10 ⁻¹	138	1	0.5	10 ⁻¹	193	10 ²	0	10 ⁻¹	248
10 ⁻⁶	3	1	29	10 ⁻⁴	2	1	84	10 ⁻²	1	1	139	1	0.5	1	194	10 ²	0	1	249
10 ⁻⁶	3	2	30	10 ⁻⁴	2	2	85	10 ⁻²	1	2	140	1	0.5	2	195	10 ²	0	2	250
10 ⁻⁶	2	10 ⁻³	31	10 ⁻⁴	1	10 ⁻³	86	10 ⁻²	0.5	10 ⁻³	141	1	0	10 ⁻³	196	10 ³	3	10 ⁻³	251
10 ⁻⁶	2	10 ⁻²	32	10 ⁻⁴	1	10 ⁻²	87	10 ⁻²	0.5	10 ⁻²	142	1	0	10 ⁻²	197	10 ³	3	10 ⁻²	252
10 ⁻⁶	2	10 ⁻¹	33	10 ⁻⁴	1	10 ⁻¹	88	10 ⁻²	0.5	10 ⁻¹	143	1	0	10 ⁻¹	198	10 ³	3	10 ⁻¹	253
10 ⁻⁶	2	1	34	10 ⁻⁴	1	1	89	10 ⁻²	0.5	1	144	1	0	1	199	10 ³	3	1	254
10 ⁻⁶	2	2	35	10 ⁻⁴	1	2	90	10 ⁻²	0.5	2	145	1	0	2	200	10 ³	3	2	255
10 ⁻⁶	1	10 ⁻³	36	10 ⁻⁴	0.5	10 ⁻³	91	10 ⁻²	0	10 ⁻³	146	10	3	10 ⁻³	201	10 ³	2	10 ⁻³	256
10 ⁻⁶	1	10 ⁻²	37	10 ⁻⁴	0.5	10 ⁻²	92	10 ⁻²	0	10 ⁻²	147	10	3	10 ⁻²	202	10 ³	2	10 ⁻²	257
10 ⁻⁶	1	10 ⁻¹	38	10 ⁻⁴	0.5	10 ⁻¹	93	10 ⁻²	0	10 ⁻¹	148	10	3	10 ⁻¹	203	10 ³	2	10 ⁻¹	258
10 ⁻⁶	1	1	39	10 ⁻⁴	0.5	1	94	10 ⁻²	0	1	149	10	3	1	204	10 ³	2	1	259
10 ⁻⁶	1	2	40	10 ⁻⁴	0.5	2	95	10 ⁻²	0	2	150	10	3	2	205	10 ³	2	2	260
10 ⁻⁶	0.5	10 ⁻³	41	10 ⁻⁴	0	10 ⁻³	96	10 ⁻¹	3	10 ⁻³	151	10	2	10 ⁻³	206	10 ³	1	10 ⁻³	261
10 ⁻⁶	0.5	10 ⁻²	42	10 ⁻⁴	0	10 ⁻²	97	10 ⁻¹	3	10 ⁻²	152	10	2	10 ⁻²	207	10 ³	1	10 ⁻²	262
10 ⁻⁶	0.5	10 ⁻¹	43	10 ⁻⁴	0	10 ⁻¹	98	10 ⁻¹	3	10 ⁻¹	153	10	2	10 ⁻¹	208	10 ³	1	10 ⁻¹	263
10 ⁻⁶	0.5	1	44	10 ⁻⁴	0	1	99	10 ⁻¹	3	1	154	10	2	1	209	10 ³	1	1	264
10 ⁻⁶	0.5	2	45	10 ⁻⁴	0	2	100	10 ⁻¹	3	2	155	10	2	2	210	10 ³	1	2	265
10 ⁻⁶	0	10 ⁻³	46	10 ⁻³	3	10 ⁻³	101	10 ⁻¹	2	10 ⁻³	156	10	1	10 ⁻³	211	10 ³	0.5	10 ⁻³	266
10 ⁻⁶	0	10 ⁻²	47	10 ⁻³	3	10 ⁻²	102	10 ⁻¹	2	10 ⁻²	157	10	1	10 ⁻²	212	10 ³	0.5	10 ⁻²	267
10 ⁻⁶	0	10 ⁻¹	48	10 ⁻³	3	10 ⁻¹	103	10 ⁻¹	2	10 ⁻¹	158	10	1	10 ⁻¹	213	10 ³	0.5	10 ⁻¹	268
10 ⁻⁶	0	1	49	10 ⁻³	3	1	104	10 ⁻¹	2	1	160	10	1	1	214	10 ³	0.5	1	269
10 ⁻⁶	0	2	50	10 ⁻³	3	2	105	10 ⁻¹	2	2	160	10	1	2	215	10 ³	0.5	2	270
10 ⁻⁵	3	10 ⁻³	51	10 ⁻³	2	10 ⁻³	106	10 ⁻¹	1	10 ⁻³	161	10	0.5	10 ⁻³	216	10 ³	0	10 ⁻³	271
10 ⁻⁵	3	10 ⁻²	52	10 ⁻³	2	10 ⁻²	107	10 ⁻¹	1	10 ⁻²	162	10	0.5	10 ⁻²	217	10 ³	0	10 ⁻²	272
10 ⁻⁵	3	10 ⁻¹	53	10 ⁻³	2	10 ⁻¹	108	10 ⁻¹	1	10 ⁻¹	163	10	0.5	10 ⁻¹	218	10 ³	0	10 ⁻¹	273
10 ⁻⁵	3	1	54	10 ⁻³	2	1	109	10 ⁻¹	1	1	164	10	0.5	1	219	10 ³	0	1	274
10 ⁻⁵	3	2	55	10 ⁻³	2	2	110	10 ⁻¹	1	2	165	10	0.5	2	220	10 ³	0	2	275

NOTE. — Table 10 (11) lists the equilibrium (time-dependent) ion fraction in photoionized gas. Tables 10 and 11 are divided into numerical parts 1 – 275. Each part lists the ion fraction for a specific set of density, metallicity, and redshift, as described here.

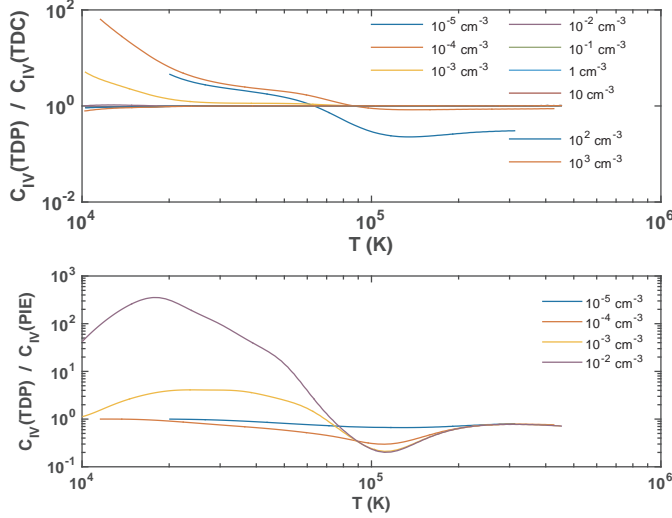


FIG. 14.— Ratio of C^{3+} TDP ion fraction and TDC ion fraction versus temperature (top panel), and ratio between C^{3+} TDP ion fraction and PIE ion fraction versus temperature (bottom panels). Different curves are for different densities.

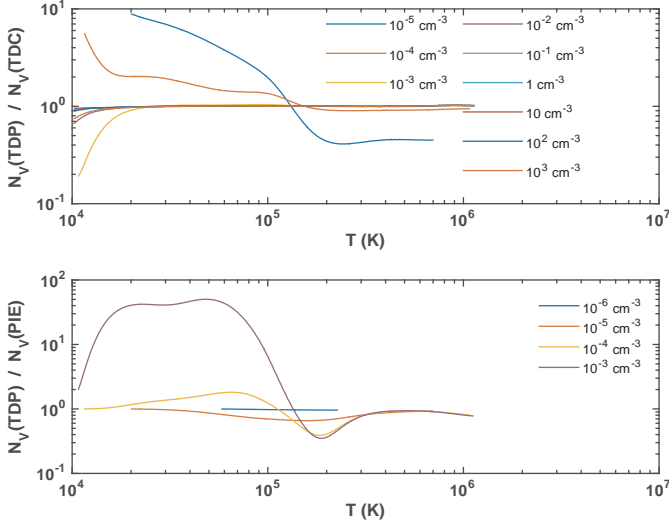


FIG. 15.— Same as Figure 14 but for N^{4+} .

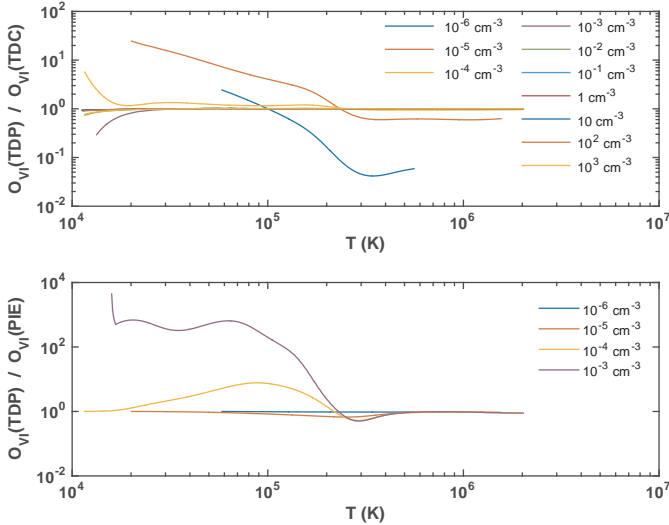


FIG. 16.— Same as Figure 14 but for O^{5+} .

TABLE 10
PHOTOIONIZATION EQUILIBRIUM ION FRACTIONS

Temperature (K)	H ⁰ /H	H ⁺ /H	He ⁰ /He	...
1.00×10^8	0.00	1.00	0.00	...
9.50×10^7	0.00	1.00	0.00	...
9.03×10^7	0.00	1.00	0.00	...
⋮	⋮	⋮	⋮	⋮

NOTE. — Table 10 is listed in its entirety in the electronic edition of the *Astrophysical Journal Supplement*. A portion is shown here for guidance. This table is divided into 275 numerical parts, each corresponding to specific density, redshift, and metallicity as described in Table 9.

TABLE 11
TIME-DEPENDENT PHOTOIONIZED ION FRACTIONS

Temperature (K)	H ⁰ /H	H ⁺ /H	He ⁰ /He	...
1.00×10^8	0.00	1.00	0.00	...
9.90×10^7	0.00	1.00	0.00	...
9.80×10^7	0.00	1.00	0.00	...
⋮	⋮	⋮	⋮	⋮

NOTE. — Table 11 is listed in its entirety in the electronic edition of the *Astrophysical Journal Supplement*. A portion is shown here for guidance. This table is divided into 275 numerical parts, each corresponding to specific density, redshift, and metallicity as described in Table 9.

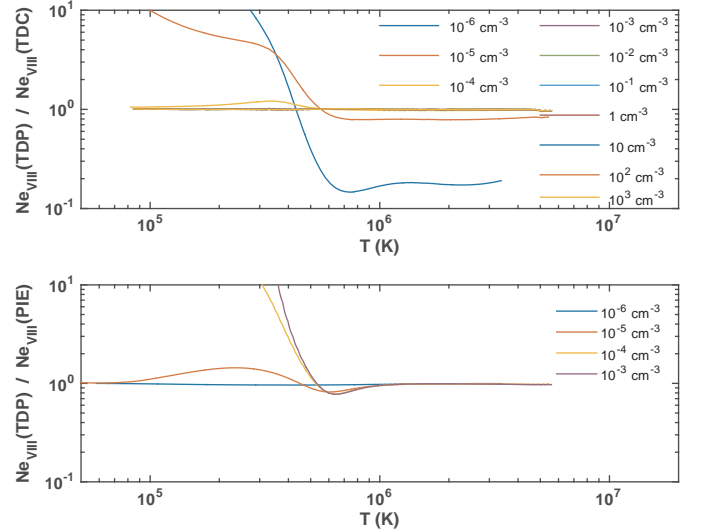


FIG. 17.— Same as Figure 14 but for Ne^{7+} .

However, as discussed above, the TDP ion fractions of certain species – which do not contribute significantly to the gas cooling – may deviate by factors of a few from the TDC or PIE ion fractions. Therefore, while the thermal evolution of TDP cooling gas may be considered to be either in PIE or TDC cooling, depending on the density, the abundance of specific species must be followed with

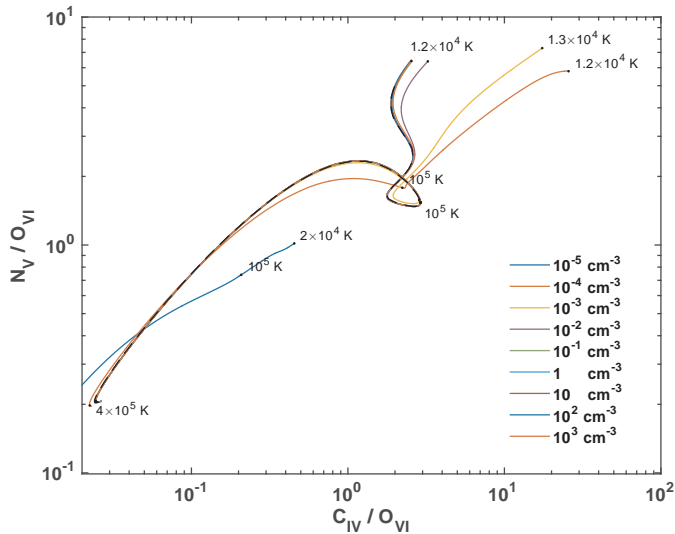


FIG. 18.— Column density ratios $N(\text{CIV})/N(\text{OVI})$ versus $N(\text{NV})/N(\text{OVI})$, for solar metallicity gas exposed to the $z = 0$ metagalactic radiation. Different solid curves are for different gas densities, as indicated in the legend. The dashed curve is for TDC cooling. As the gas cools, the column density ratios evolve from the lower left to the upper right (GS07). Some temperatures along the cooling trajectories are indicated by the dots and labels along the curves.

a full time-dependent photoionized calculation.

5. DIAGNOSTICS

Ion-ratios may be used as probes of the ionization state, temperature, metallicity, and density in photoionized cooling gas. For a uniform gas cloud, the column density ratio of the species m_i and n_j may be expressed as $\frac{N_i^m}{N_j^n} = \frac{A_m x_i(T)}{A_n x_j(T)}$ where A_e is the abundance of element e , and $x(T)$ are the ion fractions computed above.

As an example, I present in Figure 18 “cooling trajectories” for $N(\text{CIV})/N(\text{OVI})$ versus $N(\text{NV})/N(\text{OVI})$, for solar metallicity gas exposed to the $z = 0$ metagalactic radiation, for temperatures between 10^6 K and the thermal equilibrium temperature. Different gas densities are presented in Figure 18 by different curves (as indicated by the legend). For these three ions, O^{5+} is the most highly ionized, and so $N(\text{CIV})/N(\text{OVI})$ and $N(\text{NV})/N(\text{OVI})$ are small at high temperature and become large at low temperature. The absorption line ratios therefore evolve from the lower left, to the upper right. For reference, some temperature legends are displayed along the curves (dots, labels).

The cooling trajectory for TDC cooling gas is displayed by the black dashed curve. Figure 18 show that for these ratios, the cooling trajectories for TDP cooling gas with densities $\geq 10^{-1} \text{ cm}^{-3}$ are identical to the TDC cooling trajectory. At lower densities the photoionizing radiation can be seen to affect the ion ratios, especially at low temperatures, as discussed in §4. Diagnostic diagrams for other species of interest may be constructed by using the online data listed in Tables 10 and 11 above.

6. SUMMARY

In this paper I present computations of the equilibrium and non-equilibrium cooling efficiencies, heating rates, and ionization states of low-density radiatively cooling

gas exposed to external photoionizing radiation. I consider gas containing the elements H, He, C, N, O, Ne, Mg, Si, S, and Fe. In the calculations I assume cooling in the presence of the metagalactic background radiation (HM12) at redshifts 0 to 3, which photoionizes the gas and provides heating. I present results for gas temperatures, T , between 10^4 and 10^8 K, and for gas densities between 10^{-7} and 10^3 cm^{-3} . I assume that the gas is dust free, and I consider metallicities Z ranging from 10^{-3} to 2 times solar. I carry out computations including rate coefficients for all relevant atomic recombination and ionization processes, and the energy loss and gain mechanisms.

For non-equilibrium cooling, I solve the coupled time-dependent ionization and energy-budget equations for the cooling gas. For such gas I assume that the cooling is from an initially hot photoionization equilibrium state down to its thermal equilibrium temperature. The equations and numerical method are presented in §2 and Appendix A. I calculate the nonequilibrium cooling efficiencies assuming isochoric evolution (constant density), and discuss the case of isobaric evolution in §3.1.

Because I include photoionization by external radiation, both the equilibrium and time-dependent properties depend on the assumed density. The radiative cooling efficiency at a given temperature is therefore a function of both the metallicity Z and density n_{H} (or, equivalently, ionization parameter U). The results of the cooling computations are presented in Figures 4-9, and listed in Tables 4 and 5 (see Table 3 for guidance).

An important conclusion from §3 is that for every metallicity there exists a threshold density (or, equivalently, a threshold ionization parameter) below which the cooling efficiencies are close to those in photoionization equilibrium, and above which they resemble those in nonequilibrium gas with no external radiation. Above the threshold density, departures from equilibrium ionization are significant, but the impact of the photoionizing radiation may be neglected. Below this threshold density, photoionization plays a critical role, but departures from equilibrium may be neglected.

The threshold ionization parameter corresponding to $Z \gtrsim 1Z_{\odot}$ is $U = 0.42$. For $z = 0$, this corresponds to a threshold density of 10^{-5} cm^{-3} . For metallicities $\lesssim 10^{-1} Z_{\odot}$ the threshold ionization parameter is a factor of 100 lower than for solar metallicity ($U = 4.2 \times 10^{-3}$), and the threshold densities are therefore a factor of 100 higher (10^{-3} cm^{-3}). For higher redshifts, the densities corresponding to these ionization parameter are modified as the spectral energy distribution of the metagalactic background evolves. The threshold densities corresponding to $U = 0.42$ at higher redshifts are displayed in Figure 5.

The results of the equilibrium and nonequilibrium ionization calculations are presented in §4. While the thermal evolution (and the associated abundances of the major coolants) in TDP cooling gas may be considered to be either in PIE or TDC, depending on the density, the abundance of some specific species may differ by factors of a few from the TDC / PIE values, and must be followed with a full TDP cooling computation. The full data for the time-dependent photoionized ion fractions are listed in online Tables 10 and 11, as summarized in Table 9.

Ion ratios are useful as diagnostic probes. In §5 I discuss one example, $N(\text{C}_{\text{IV}})/N(\text{O}_{\text{VI}})$ versus $N(\text{N}_{\text{V}})/N(\text{O}_{\text{VI}})$, and show how this ratio evolves in photoionized cooling gas and how it varies with density for realistic nonequilibrium conditions.

APPENDIX

APPENDIX A. NUMERICAL DETAILS

The computations included in this work rely on the numerical scheme outlined in GS07 and improved in Gnat & Sternberg (2009). The details of this method are summarized here for completeness.

In this work, I consider all ionization stages of the elements H, He, C, N, O, Ne, Mg, Si, S, and Fe. The microphysical ionization and recombination processes included in this computation are photoionization (Verner et al. 1996), including multielectron Auger ionization processes (Kaastra & Mewe 1993) induced by X-ray photons, collisional ionization by thermal electrons (Voronov 1997), radiative recombination (Aldrovandi & Pequignot 1973; Shull & van Steenberg 1982; Landini & Monsignori Fossi 1990; Landini & Fossi 1991; Pequignot et al. 1991; Arnaud & Raymond 1992; Verner et al. 1996), dielectronic recombination (Aldrovandi & Pequignot 1973; Arnaud & Raymond 1992; Badnell et al. 2003; Badnell 2006; Colgan et al. 2003, 2004, 2005; Zatsarinny et al. 2003, 2004a, 2004b, 2005a, 2005b, 2006; Altun et al. 2004, 2005, 2006; Mitnik & Badnell 2004), and neutralization and ionization by charge transfer reactions with hydrogen and helium atoms and ions (Kingdon & Ferland fits³, based on Kingdon & Ferland 1996; Ferland et al. 1997; Clarke et al. 1998; Stancil et al. 1998; Arnaud & Rothenflug 1985), including the statistical charge transfer rate coefficients for high-ions with charges greater than +4 (Kingdon & Ferland 1996).

The time-dependent equations for the ion abundance fractions, x_i , of element m in ionization stage i , are

$$\begin{aligned} \frac{dx_i}{dt} = & x_{i-1} [q_{i-1}n_e + k_{\uparrow i-1}^{\text{H}}n_{\text{H}^+} + k_{\uparrow i-1}^{\text{He}}n_{\text{He}^+}] + \sum_{j<i} x_j \Gamma_{j \rightarrow i} \\ & + x_{i+1} [\alpha_{i+1}n_e + k_{\downarrow i+1}^{\text{H}}n_{\text{H}^0} + k_{\downarrow i+1}^{\text{He}}n_{\text{He}^0}] \\ & - x_i [(q_i + \alpha_i)n_e + \Gamma_i + k_{\downarrow i}^{\text{H}}n_{\text{H}^0} + k_{\downarrow i}^{\text{He}}n_{\text{He}^0} \\ & + k_{\uparrow i}^{\text{H}}n_{\text{H}^+} + k_{\uparrow i}^{\text{He}}n_{\text{He}^+}] . \end{aligned} \quad (\text{A1})$$

In this expression, q_i and α_i are the temperature-dependent rate coefficients for collisional ionization and recombination (radiative plus dielectronic), and $k_{\downarrow i}^{\text{H}}$, $k_{\downarrow i}^{\text{He}}$, $k_{\uparrow i}^{\text{H}}$, and $k_{\uparrow i}^{\text{He}}$ are the rate coefficients for charge transfer reactions with hydrogen and helium that lead to ionization or neutralization. The quantities n_{H^0} , n_{H^+} , n_{He^0} , n_{He^+} , and n_e are the particle densities (cm^{-3}) for neutral hydrogen, ionized hydrogen, neutral helium, singly ionized helium, and electrons, respectively. $\Gamma_{j \rightarrow i}$ are the local rates of photoionization of ions j which result in the ejection of $i - j$ electrons. Γ_i are the total photoionization rates of ions i due to externally incident radiation. For each element m , the ion fractions $x_i = n_{i,m}/(n_{\text{H}}A_m)$ must at all times satisfy $\sum x_i = 1$.

The ionization equations (A1) and energy balance equation (4) form a set of 103 coupled ordinary differential equations (ODEs). I use a Livermore ODE solver (Hindmarsh 1983) to integrate these equations. This solver integrates both stiff and nonstiff ODE systems, and transitions automatically between stiff and nonstiff solution methods as necessary (see <http://www.netlib.org/odepack/>). Along the solution, the pressure is advanced in small steps, $\Delta P = \varepsilon P$, where P is the current gas pressure, and $\varepsilon \lesssim 0.05$. These small pressure steps are associated with small time steps Δt , using equation 4. Over the small time step Δt , the pressure is assumed to evolve linearly with time. The cooling efficiencies and heating rates at each point are computed using Cloudy (ver. 13.00), given the local nonequilibrium ion-fractions. When integrating, the local errors for hydrogen, helium, and metal ion-fractions were set to be smaller than 10^{-9} , 10^{-8} , and 10^{-7} , respectively. The accuracy is higher than that used in GS07, because heating is sometimes dominated by trace species. This point is further discussed in Appendix B.

I verify convergence by repeating the computation at a higher resolution (i.e. smaller ε) and confirming that the resulting cooling and heating rates and ion fractions as functions of time remain unaltered. I have carried out the integration of the ionization and energy-balance equations down to the thermal equilibrium temperature, at which point cooling will cease. However, if the thermal equilibrium temperature is lower than 10^4 K, I stop the computation at $T_{\text{low}} = 10^4$ K, because molecular chemistry and dust cooling, which are not included in this work, may significantly affect the results at lower temperatures.

APPENDIX B. THE ROLE OF X-RAY HEATING

This Appendix considers the role that extreme X-ray radiation plays in setting the heating rates in dilute plasmas (e.g. Madau & Efstathiou 1999, Hambrick et al. 2011).

In order to examine the importance of high-energy photons for the energy budget in low-density gases, we considered the PIE heating rates under the influence of the HM12 metagalactic background radiation. First I consider the heating rates used throughout this paper, namely by the HM12 background up to an energy of 8,330 keV. Then I considered the HM12 background truncated at an energy of 41 keV. The PIE rates were computed using Cloudy, assuming equilibrium conditions, and taking into account the Klein-Nishina corrections (G. Ferland, private communication).

In figure 19, I plot the ratio between the heating rates, $\Upsilon(J_{0.12 \text{ eV}-8330 \text{ keV}})/\Upsilon(J_{0.12 \text{ eV}-41 \text{ keV}})$. I consider five

³ See <http://www-cfadc.phy.ornl.gov/astro/ps/data/cx/hydrogen/rates/ct.html>.

different values of metallicity, $Z = 2, 1, 10^{-1}, 10^{-2}$, and 10^{-3} time solar, (top to bottom rows), and three different values of redshift, $z = 0, 1$, and 2 (from left to right). For each metallicity-redshift combination, I display the ratio $\Upsilon(J_{0.12 \text{ eV}-8330 \text{ keV}})/\Upsilon(J_{0.12 \text{ eV}-41 \text{ keV}})$ in PIE as a function of density (horizontal axis) and temperature (vertical axis). The ratio is indicated by the color-map, and by the labeled contours.

Figure 19 shows that at low temperatures and high densities (lower right in each panel) the X-ray radiation has a negligible contribution to the heating rate. However, at low densities and high temperatures (upper left), X-ray heating plays an important role, and including the $40 - 8,330 \text{ keV}$ radiation, may raise the heating rates by factors up to ~ 2 . For $Z \gtrsim 1Z_{\odot}$ (two upper rows), extreme-X-ray heating only becomes important at highly rarified environments (with densities below the cosmic mean, $n \lesssim 10^{-7} \text{ cm}^{-3}$), and extremely high temperatures ($T \gtrsim 10^7 \text{ K}$). For typical WHIM densities and metallicities ($Z \sim 0.1Z_{\odot}$), extreme-X ray heating contributes to the heating budget for temperatures above a few $\times 10^6 \text{ K}$. For primordial plasma, it contributes above $\sim 10^6 \text{ K}$. Figure 19 shows that in order to accurately estimate the heating rates in hot dilute plasmas, we need a solid knowledge regarding the intensity (and SED) of the extreme X-ray radiation.

Note, however, that while the absolute heating rate estimates should be taken with a grain of salt, our understanding of the thermal evolution of low-density gas is insensitive to details of the extreme X-ray radiation: The solid curve in each panel of Figure 19 shows, for each density, the photoionization equilibrium temperature at which cooling is exactly balanced by heating (computed here using the $0.12 \text{ eV} - 8330 \text{ keV}$ radiation). The dashed curves show, for each density, the temperature for which the heating falls an order of magnitude below cooling. Therefore, in the region to the upper right of the dashed line, heating is orders of magnitude lower than cooling. Below the dashed line, the exact value of the heating rate is important for the thermal evolution of the gas. In particular, it is important for determining the value of the equilibrium temperatures.

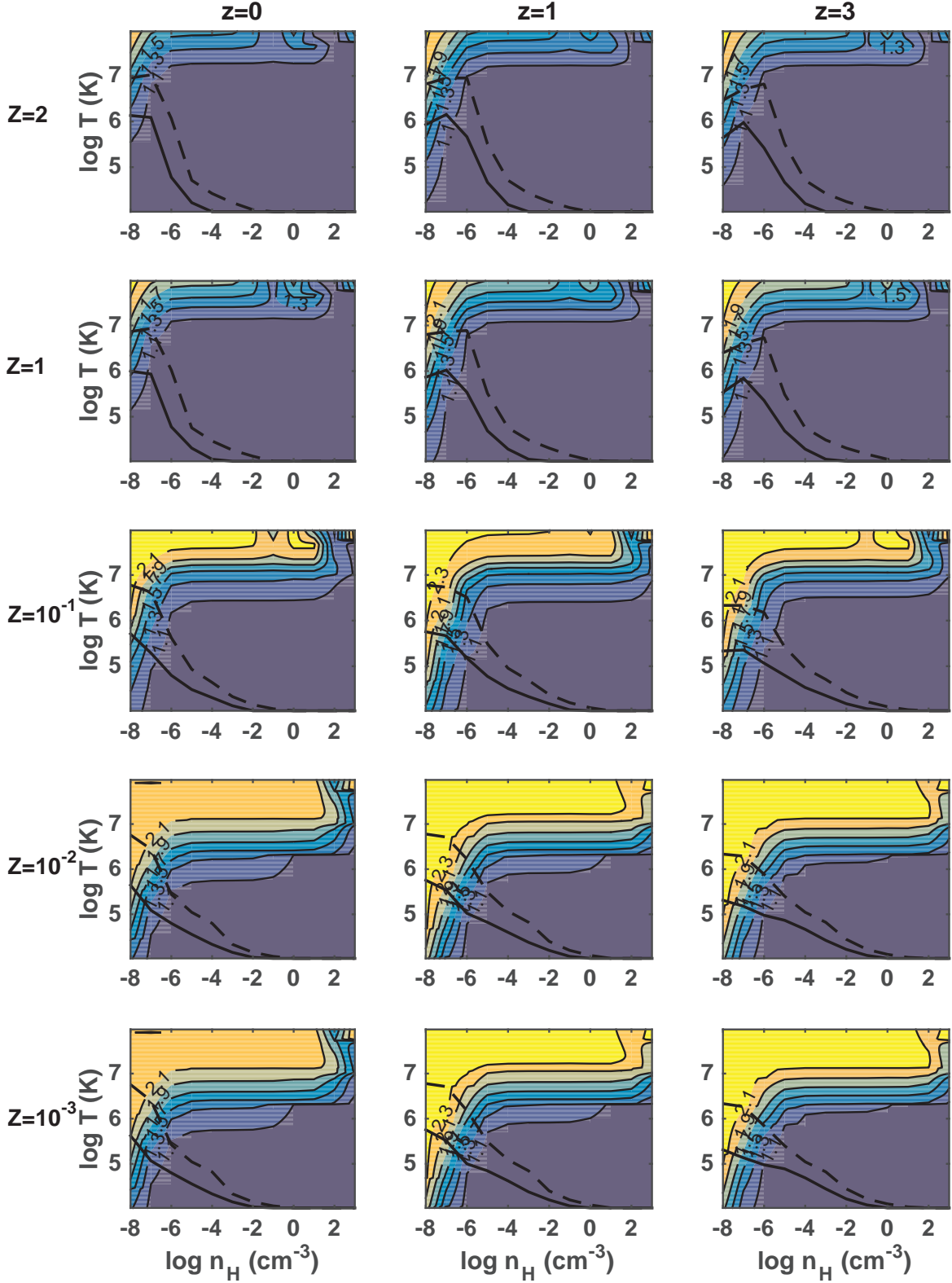
This demonstrates that within most of the region for which the ratio $\Upsilon(J_{0.12 \text{ eV}-8330 \text{ keV}})/\Upsilon(J_{0.12 \text{ eV}-41 \text{ keV}})$ is large, the heating has a negligible impact on the thermal evolution of the plasma because it is orders of magnitude lower than the cooling. The X-ray radiation therefore only affects the thermal properties of the plasma when the value of $\Upsilon(J_{0.12 \text{ eV}-8330 \text{ keV}})/\Upsilon(J_{0.12 \text{ eV}-41 \text{ keV}})$ is large *and* heating is comparable to cooling (i.e. below the dashed line). Figure 19 demonstrates that both conditions apply for low metallicity gas ($Z \lesssim 10^{-1}Z_{\odot}$) at extremely low densities ($n_{\text{H}} \lesssim 10^{-6} \text{ cm}^{-3}$). At these densities, the cooling times are longer than a Hubble time, even for the less energetic SED (truncated at 40 keV). For physically relevant parameters (for which the cooling times are shorter than a Hubble time), the exact details of the X-ray background are not expected to significantly affect the thermal evolution of the gas.

ACKNOWLEDGMENTS

This research was supported by the Israeli Centers of Excellence (I-CORE) program (center no. 1829/12); by the Israel Science Foundation (grant No. 857/14); and by program AR-12655 provided by NASA through a grant from the STScI, under NASA contract NAS5-26555.

REFERENCES

- Aldrovandi, S. M. V., & Pequignot, D. 1973, *A&A*, 25, 137
 Altun, Z., Yumak, A., Badnell, N. R., Colgan, J., & Pindzola, M. S. 2004, *A&A*, 420, 775
 Altun, Z., Yumak, A., Badnell, N. R., Colgan, J., & Pindzola, M. S. 2005, *A&A*, 433, 395
 Altun, Z., Yumak, A., Badnell, N. R., Loch, S. D., & Pindzola, M. S. 2006, *A&A*, 447, 1165
 Arnaud, M., & Raymond, J. 1992, *ApJ*, 398, 394
 Arnaud, M., & Rothenflug, R. 1985, *A&AS*, 60, 425
 Asplund, M., Grevesse, N., & Sauval, A. J. 2005, *ASP Conf. Ser. 336: Cosmic Abundances as Records of Stellar Evolution and Nucleosynthesis*, 336, 25
 Badnell, N. R., O’Mullane, M. G., Summers, H. P., et al. 2003, *A&A*, 406, 1151
 Badnell, N. R. 2006, *A&A*, 447, 389
 Ballantyne, D. R., Ferland, G. J., & Martin, P. G. 2000, *ApJ*, 536, 773
 Benson, A. J., Lacey, C. G., Baugh, C. M., Cole, S., & Frenk, C. S. 2002a, *MNRAS*, 333, 156
 Benson, A. J., Frenk, C. S., Lacey, C. G., Baugh, C. M., & Cole, S. 2002b, *MNRAS*, 333, 177
 Benson, A. J., Frenk, C. S., Baugh, C. M., Cole, S., & Lacey, C. G. 2003, *MNRAS*, 343, 679
 Cantalupo, S. 2010, *MNRAS*, 403, L16
 Churchill, C. W., Klimek, E., Medina, A., & Vander Vliet, J. R. 2014, *arXiv:1409.0916*
 Churchill, C. W., Vander Vliet, J. R., Trujillo-Gomez, S., Kacprzak, G. G., & Klypin, A. 2015, *ApJ*, 802, 10
 Badnell, N. R., O’Mullane, M. G., Summers, H. P., et al. 2003, *A&A*, 406, 1151
 Badnell, N. R. 2006, *A&A*, 447, 389
 Clarke, N. J., Stancil, P. C., Zygelman, B., & Cooper, D. L. 1998, *Journal of Physics B Atomic Molecular Physics*, 31, 533
 Colgan, J., Pindzola, M. S., Whiteford, A. D., & Badnell, N. R. 2003, *A&A*, 412, 597
 Colgan, J., Pindzola, M. S., & Badnell, N. R. 2004, *A&A*, 417, 1183
 Colgan, J., Pindzola, M. S., & Badnell, N. R. 2005, *A&A*, 429, 369
 Crighton, N. H. M., Hennawi, J. F., Simcoe, R. A., et al. 2015, *MNRAS*, 446, 18
 Drake, J. J., & Testa, P. 2005, *Nature*, 436, 525
 Efstathiou, G. 1992, *MNRAS*, 256, 43P
 Feldmann, R., & Mayer, L. 2015, *MNRAS*, 446, 1939
 Ferland, G. J., Korista, K. T., Verner, D. A., & Dalgarno, A. 1997, *ApJ*, 481, L115
 Gnat, O., & Sternberg, A. 2007, *ApJS*, 168, 213
 Gnat, O., & Sternberg, A. 2009, *ApJ*, 693, 1514
 Gnedin, N. Y., & Hollon, N. 2012, *ApJS*, 202, 13
 Haardt, F., & Madau, P. 2012, *ApJ*, 746, 125
 Hambrick, D. C., Ostriker, J. P., Johansson, P. H., & Naab, T. 2011, *MNRAS*, 413, 2421
 Hindmarsh, A. C. 1983, in *Scientific Computing*, ed. R. S. Stepleman et al. (Amsterdam: North-Holland), 55
 Kaastra, J. S., & Mewe, R. 1993, *A&AS*, 97, 443
 Kafatos, M. 1973, *ApJ*, 182, 433
 Kingdon, J. B., & Ferland, G. J. 1996, *ApJS*, 106, 205
 Landini, M., & Monsignori Fossi, B. C. 1990, *A&AS*, 82, 229
 Landini, M., & Fossi, B. C. M. 1991, *A&AS*, 91, 183
 Madau, P., & Efstathiou, G. 1999, *ApJ*, 517, L9
 Mitnik, D. M., & Badnell, N. R. 2004, *A&A*, 425, 1153
 McCray, R. A. 1987, *Spectroscopy of Astrophysical Plasmas*, 255
 Navarro, J. F., & Steinmetz, M. 1997, *ApJ*, 478, 13
 Oppenheimer, B. D., & Schaye, J. 2013, *MNRAS*, 434, 1063
 Pequignot, D., Petitjean, P., & Boisson, C. 1991, *A&A*, 251, 680
 Puchwein, E., Bolton, J. S., Haehnelt, M. G., et al. 2015, *MNRAS*, 450, 4081
 Richings, A. J., & Schaye, J. 2015, *arXiv:1506.08829*
 Shull, J. M., & van Steenberg, M. 1982, *ApJS*, 48, 95
 Stancil, P. C., Havener, C. C., Krstić, P. S., et al. 1998, *ApJ*, 502, 1006



- Thompson, T. A., Quataert, E., Zhang, D., & Weinberg, D. H. 2016, *MNRAS*, 455, 1830
- Turner, M. L., Schaye, J., Steidel, C. C., Rudie, G. C., & Strom, A. L. 2015, *MNRAS*, 450, 2067
- Vasiliev, E. O. 2011, *MNRAS*, 414, 3145
- Verner, D. A., Ferland, G. J., Korista, K. T., & Yakovlev, D. G. 1996, *ApJ*, 465, 487
- Voronov, G. S. 1997, *Atomic Data and Nuclear Data Tables*, 65, 1
- Weinberg, D. H., Hernquist, L., & Katz, N. 1997, *ApJ*, 477, 8
- White, S. D. M., & Rees, M. J. 1978, *MNRAS*, 183, 341
- Wiersma, R. P. C., Schaye, J., & Smith, B. D. 2009, *MNRAS*, 393, 99
- Zatsarinny, O., Gorczyca, T. W., Korista, K. T., Badnell, N. R., & Savin, D. W. 2003, *A&A*, 412, 587
- Zatsarinny, O., Gorczyca, T. W., Korista, K. T., Badnell, N. R., & Savin, D. W. 2004a, *A&A*, 417, 1173
- Zatsarinny, O., Gorczyca, T. W., Korista, K., Badnell, N. R., & Savin, D. W. 2004b, *A&A*, 426, 699
- Zatsarinny, O., Gorczyca, T. W., Korista, K. T., et al. 2005a, *A&A*, 438, 743
- Zatsarinny, O., Gorczyca, T. W., Korista, K. T., et al. 2005b, *A&A*, 440, 1203
- Zatsarinny, O., Gorczyca, T. W., Fu, J., et al. 2006, *A&A*, 447, 379